nature chemical biology

ARTICLES

https://doi.org/10.1038/s41589-022-01135-y

Check for updates

Engineered LwaCas13a with enhanced collateral activity for nucleic acid detection

Jie Yang[1,10], Yang Song[2,3,10], Xiangyu Deng[4], Jeffrey A. Vanegas[1], Zheng You[1], Yuxuan Zhang[2,3], Zhengyan Weng[2,3], Lori Avery[5], Kevin D. Dieckhaus[6], Advaith Peddi[4], Yang Gao[4] ✉, Yi Zhang[2,7] ✉ and Xue Gao[1,8,9] ✉

Clustered regularly interspaced short palindromic repeats (CRISPR)–CRISPR-associated protein 13 (Cas13) has been rapidly developed for nucleic-acid-based diagnostics by using its characteristic collateral activity. Despite the recent progress in optimizing the Cas13 system for the detection of nucleic acids, engineering Cas13 protein with enhanced collateral activity has been challenging, mostly because of its complex structural dynamics. Here we successfully employed a novel strategy to engineer the *Leptotrichia wadei* (Lwa)Cas13a by inserting different RNA-binding domains into a unique active-site-proximal loop within its higher eukaryotes and prokaryotes nucleotide-binding domain. Two LwaCas13a variants showed enhanced collateral activity and improved sensitivity over the wild type in various buffer conditions. By combining with an electrochemical method, our variants detected the SARS-CoV-2 genome at attomolar concentrations from both inactive viral and unextracted clinical samples, without target preamplification. Our engineered LwaCas13a enzymes with enhanced collateral activity are ready to be integrated into other Cas13a-based platforms for ultrasensitive detection of nucleic acids.

Cas13 orthologs, the single effectors of the Class 2 type VI clustered regularly interspaced short palindromic repeats (CRISPR)–CRISPR-associated protein (Cas) systems, are RNA-guided ribonucleases[1]. The CRISPR RNAs (crRNAs) of this family contain a direct repeat stem loop that interacts with the Cas13 protein to form an RNase-inactive binary complex and a spacer sequence that base pairs with the target RNA[2]. The resulting Cas13–crRNA–target ternary complex undergoes a large-scale conformational change in which two higher eukaryotes and prokaryotes nucleotide-binding (HEPN) domains move toward each other to form a single catalytic pocket to cleave the target RNA. Intriguingly, this catalytic pocket localized on the outer surface of the target-activated Cas13 complex can non-specifically cleave any surrounding RNA molecules in a characteristic 'collateral effect'[2]. This target-triggered collateral activity, originally an immune defense mechanism intended to induce host dormancy and prevent the propagation of invading phages, has been rapidly developed for in vitro detection of nucleic acids[3]. For example, the Cas13–crRNA surveillance complex is activated upon target recognition and performs collateral cleavage of nearby dye–quencher pairs linked by single-stranded RNA (ssRNA)[3,4] to rapidly generate measurable fluorescent or colorimetric signals[3–5].

The *Leptotrichia wadei* (Lwa)Cas13a has been widely used in nucleic-acid-based diagnostics. Coupling LwaCas13a collateral activity to target preamplification, the specific high-sensitivity enzymatic reporter unlocking (SHERLOCK) platform has detected attomolar levels of viral RNA and other endogenous RNA targets[3]. Combining LwaCas13a with auxiliary Csm6 endoribonuclease, SHERLOCKv2 shortened the detection time for a Dengue RNA target[4]. Integrating SHERLOCK detection with colorimetric barcoding technology, the CARMEN system achieved multiplexed detection of thousands of human virus samples[6]. A LwaCas13a-based COVID-19 diagnostic test has undergone clinical validation[7] and received U.S. Food and Drug Administration Emergency Use Authorization during the pandemic[8]. Although target preamplification can provide high-concentration samples for CRISPR-based detection of nucleic acids, this procedure normally requires multiple liquid-transfer steps and takes 2 h for column-based isolation of nucleic acids and isothermal amplification of nucleic acid[8,9], leading to possible cross-contamination and RNA degradation. Moreover, non-specific isothermal amplification was reported to occur at a high frequency[10], increasing the risk of false-positive testing[8–12]. Without target preamplification, LwaCas13a can detect short microRNA targets at concentrations as low as 2 pM by integrating electrochemical microfluidic chips[13] and can also detect SARS-CoV-2 targets at low femtomolar levels when coupled with a photolithography-fabricated microchamber array and three crRNAs[14]. However, amplification-free detection of nucleic acids at the attomolar level is necessary for accurate and field-deployable diagnosis to ensure timely identification of pathogens and prevent infection transmission, as well as broader applications in biological assessments and environmental surveillance[15]. Although *Leptotrichia buccalis* (Lbu)Cas13a was reported to have higher sensitivity for detection of nucleic acids[16,17], it was promiscuous in the presence or absence of the target RNA in a spacer- and reporter-sequence-dependent manner[4].

Despite the recent efforts to improve Cas13a-based detection of nucleic acids[3–8,13,14,16–18], engineering Cas13a protein with enhanced

[1]Department of Chemical and Biomolecular Engineering, Rice University, Houston, TX, USA. [2]Department of Biomedical Engineering, University of Connecticut, Storrs, CT, USA. [3]Institute of Materials Science, University of Connecticut, Storrs, CT, USA. [4]Department of Biosciences, Rice University, Houston, TX, USA. [5]Department of Pathology and Laboratory Medicine, UConn Health, Farmington, CT, USA. [6]Division of Infectious Diseases, Department of Medicine, UConn Health, Farmington, CT, USA. [7]Polymer Program, Institute of Materials Science, University of Connecticut, Storrs, CT, USA. [8]Department of Bioengineering, Rice University, Houston, TX, USA. [9]Department of Chemistry, Rice University, Houston, TX, USA. [10]These authors contributed equally: Jie Yang, Yang Song. ✉e-mail: yg60@rice.edu; yi.5.zhang@uconn.edu; xue.gao@rice.edu

collateral activity has been challenging and it has not yet been successful, possibly because of the dynamic nature and the structural complexity of the RNase-active Cas13a enzymes. Here we employed a structural analysis of LwaCas13a to guide a novel protein engineering strategy designed to improve its collateral activity. We fused different types of RNA-binding domains (RBDs) to the tip of a unique β-hairpin loop proximal to the LwaCas13a active site to increase its RNA substrate binding affinity. We found that four of the seven RBD–LwaCas13a loop fusions enhanced the collateral activity and two of them (RBD#3L and RBD#4L) greatly improved the detection sensitivity for different targets, including SARS-CoV-2, Zika, Dengue, and Ebola virus RNA, as well as microRNAs. By coupling our collateral-activity-enhanced LwaCas13a to an electrochemical sensor, we successfully achieved ~1 attomolar (aM) sensitivity and amplification-free detection for heat-inactivated SARS-CoV-2 genomic RNA and accurately detected clinical positive SARS-CoV-2 samples with a viral load as low as 12 copies per microliter (20 aM) in the reaction, without RNA extraction and preamplification steps. Our results show the potential of this approach for ultrasensitive detection of a wide range of RNA targets with clinical, biological, and environmental importance.

Results

Tether RBDs to the N or C terminus of LwaCas13a. To enhance the collateral activity of LwaCas13a, we first aimed to strengthen the interactions with its RNA substrates. We hypothesized that fusing an RBD to Cas13a protein could facilitate the capture of adjacent target and reporter RNAs. We thus chose seven RBDs with different topologies[19–26] as candidates, including the adenosine deaminases acting on RNA 1 (ADAR1) double-stranded RNA (dsRNA)-binding motif 3 (DRBM3, RBD#1)[21], heterogeneous nuclear ribonucleoprotein (hnRNP) A1 RNA-recognition motif 1 (RRM1, RBD#2), RRM2 (RBD#3)[22], hnRNP C RRM (RBD#4)[23], methyltransferase-like 3 (METTL3) zinc-finger domain (ZnF, RBD#5)[24], ADAR1 Z-DNA/RNA-binding domain α (Zα, RBD#6), and β (Zβ, RBD#7)[25,26] (Fig. 1a and Supplementary Table 1).

RBDs were tethered either to the N or C terminus of LwaCas13a via a 32-residue XTEN linker to allow the mobility of the RBD (Fig. 1a). We expressed and purified the resulting 14 RBD fusions, and tested their collateral activities in the presence of a synthetic SARS-CoV-2 N gene fragment (Fig. 1b,c and Extended Data Fig. 1). A comparison of the 30-min-endpoint fluorescence signals produced by the wild-type (WT) and RBD fusions showed that RBD#4N and RBD#6N slightly increased the endpoint fluorescent signal by 75.8% and 32.5%, respectively, while fluorescence signals produced by all other RBD fusions were similar to or less than that of the WT (Fig. 1b,c and Extended Data Fig. 1). We then employed RoseTTAFold[27] to generate a LwaCas13a structure model (Fig. 2a,b) on the basis of the crystal structure of LbuCas13a[2] (Protein Data Bank (PDB) ID: 5XWP; 80% identity). This model indicated that the N terminus of LwaCas13a may be buried within the crRNA-binding cleft, while the C terminus may be very close to the catalytic center of the protein. Thus, linking RBDs to the N or C terminus could disrupt Cas13a folding or active-site configuration, providing a possible explanation as to why 9 of the 14 RBD fusions led to decreased activity (Fig. 1b,c).

Identify Cas13a active-site-proximal loops for RBD insertions. By carefully examining the LwaCas13a structure model, we identified a unique β-hairpin loop G410–G425 (Loop 1) within the HEPN1 domain located above the active-site cleft (Fig. 2b,c). We envisioned that Loop 1 could be an optimal insertion site for the proper orientation of RBDs to enhance RNA binding to the protein. We thus fused the seven selected RBDs between residues N415 and N416 at the tip of Loop 1 (Fig. 2c) without linkers (owing to the high flexibility of Loop 1), and tested the collateral activity of the purified fusion proteins using the same conditions as in Fig. 1b,c. Five of the Loop 1 RBD fusions (RBD#1L, #2L, #3L, #4L, and #6L) had 59%, 216%, 468%, 518%, and 174% higher endpoint fluorescence signals than the WT after 30 min exposure to the synthetic SARS-CoV-2 N gene RNA target (Fig. 2d). We also observed similar collateral activity improvement with two other synthetic RNA targets, where RBD#2L, #3L, #4L, and #6L revealed 164%, 264%, 241%, and 171% increased activity relative to WT with a synthetic SARS-CoV-2 RdRp gene target and 59%, 102%, 91%, and 38% enhanced activity with a ssRNA1 target[3] (Extended Data Fig. 2a–c). The 99-amino-acid hnRNP A1 RRM2 (Fig. 2e) and 105-amino-acid hnRNP C RRM (Fig. 2f) Loop 1 fusions (named RBD#3L and #4L) showed the highest collateral activities for all three tested synthetic RNA targets.

We reasoned that RBD insertion position might affect its orientation and RNA substrate capture, so we varied its insertions between amino acids N415, N416, and K417 near the tip of Loop 1 and beyond its β-sheet secondary structure (Fig. 2c). As other RBD#3 and #4 Loop 1 fusions also demonstrated significantly increased collateral activity over the WT, insertion between amino acid residue N415 and N416 (RBD#3L and #4L) exhibited comparable or higher collateral activities among all tested insertion sites (Fig. 2g and Extended Data Fig. 2d–f). Additionally, inserting tandem RBDs, that is, RBD#3–linker–RBD#4 or RBD#4–linker–RBD#3 into the same position did not further improve collateral activity (Extended Data Fig. 2g,h). By contrast, RBD #3 and #4 insertions at another active-site-proximal loop within the HEPN2 domain of LwaCas13a (Loop 2, N992–G1004; Fig. 2a–c) led to a complete loss of collateral activity, even after the addition of flexible GSSG or $(GGGGS)_3$ linkers (Fig. 2g). Collectively, inserting RBDs to the optimal site in Loop 1 resulted in two LwaCas13a variants, RBD#3L and #4L, with the highest collateral activity improvement.

Reporter length requirement for optimal collateral cleavage. Further analyzing the structure model, we estimated the distance between the tip of Loop 1 (N415) and the LwaCas13a catalytic residues to be approximately 35 Å. Although this distance might vary owing to the flexibility of Loop 1, an RNA reporter with a length over ten nucleotides would effectively span the distance between the RBD-binding site and the HEPN active site. Additionally, the hnRNP A1 RRM2 (RBD#3; Fig. 2e) binds at least four nucleotides with a minimal sequence preference[22], while the hnRNP C RRM (RBD#4; Fig. 2f) preferably binds tracts of four uridines[23]. Thus, the seven-nucleotide RNaseAlert substrate used in our above assays could be suboptimal owing to its insufficient length. Moreover, LwaCas13a has a U–U preference for collateral cleavage[4], and replacement of the RNaseAlert with a PolyU-linked fluorophore–quencher pair improves WT collateral activity[28].

With this knowledge, we tested the collateral activity of target-bound RBD#3L, RBD#4L, and WT with 5′-6-carboxyfluorescein (6-FAM)-labeled-PolyU reporters of four different lengths: 5, 11, 15, and 20 nucleotides. Reactions were initiated by incubation with the synthetic SARS-CoV-2 N gene fragment. Aliquots were collected at 0, 5, 10, 15, and 30 min and resolved on a denaturing gel to visualize the time course of collateral cleavage activity (Extended Data Fig. 3). RBD#3L, RBD#4L, and the WT all showed increased reporter cleavage in a reporter-length-dependent manner. Densitometry analysis of the cleaved products exhibited more efficient collateral cleavage by RBD#3L and RBD#4L than WT in reactions using U_{11}, U_{15}, or U_{20}, but not U_5 reporters (Fig. 3a,b and Extended Data Fig. 3). We further quantified the cleavage activity of RBD#3L, #4L, and the WT by using the self-quenched U_5, RNaseAlert (N_7), and U_{11} reporters (Fig. 3c,d). The overall fluorescence intensity and initial collateral cleavage rates of all three proteins were the lowest when RNaseAlert (N_7) was used, possibly owing to the U–U preference of LwaCas13a. By using the

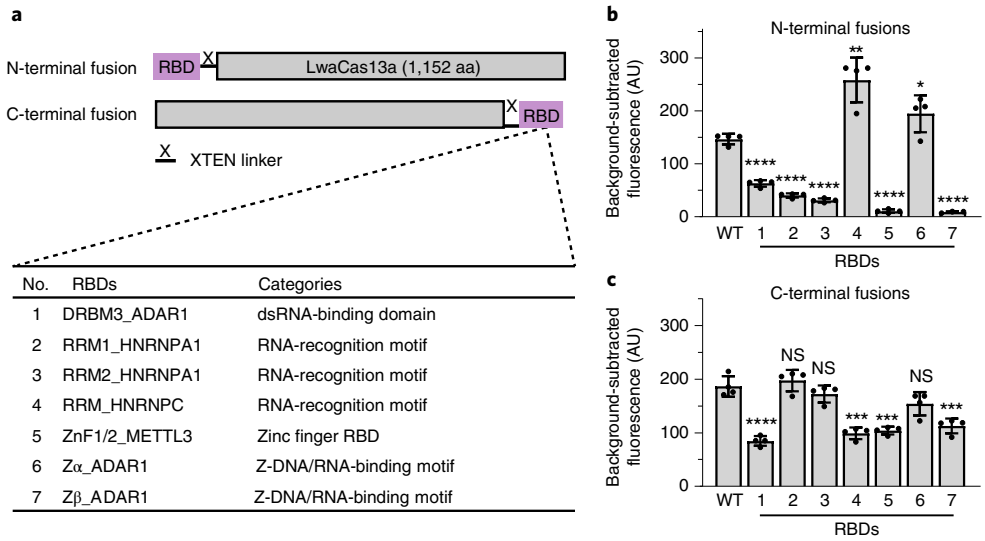

No.	RBDs	Categories
1	DRBM3_ADAR1	dsRNA-binding domain
2	RRM1_HNRNPA1	RNA-recognition motif
3	RRM2_HNRNPA1	RNA-recognition motif
4	RRM_HNRNPC	RNA-recognition motif
5	ZnF1/2_METTL3	Zinc finger RBD
6	Zα_ADAR1	Z-DNA/RNA-binding motif
7	Zβ_ADAR1	Z-DNA/RNA-binding motif

Fig. 1 | Design of N- and C-terminal RBD fusions to LwaCas13a. a, Seven RBDs were selected and fused to LwaCas13a at the N or C terminus with a flexible XTEN linker (32 amino acids). **b**,**c**, Background-subtracted fluorescence comparing the collateral activity between WT and RBD#1N–#7N (**b**), and between WT and RBD#1C–#7C (**c**). For **b**,**c**, 10 pM of synthetic SARS-CoV-2 N gene fragment targets (T1) were detected by WT and its N or C fusion variants. The background-subtracted fluorescence (arbitrary units, AU) was calculated by taking the raw fluorescence signal of the testing sample and subtracting that of the corresponding non-target control, in which the target RNA was replaced by nuclease-free water. Each bar was plotted from four technical replicates with standard error of means (s.e.m.) at an assay time of 30 min. Two-tailed *P* values were calculated using unpaired *t*-tests: $^{*}P = 0.04$; $^{**}P = 0.0022$; $^{***}P = 0.0008$ for RBD#7C, $P = 0.0002$ for both RBD#4 C and #5 C; and $^{****}P < 0.0001$; compared to WT (see Source Data for *P* values). NS, not significant.

U_{11} reporter, WT, RBD#3L and #4L initial collateral cleavage rates were 1.5-, 4.7-, and 5.8-fold higher than those of the U_5 reporter, showing a reporter length requirement for the optimal collateral activity of RBD fusions higher than that of the WT (Fig. 3c,d). Further optimizing reaction buffer compositions (Supplementary Figs 1 and 2) improved the analytical limit-of-detection (LoD) of the WT to ~0.3 pM (final concentration in the reaction), while RBD#3L and RBD#4L reached the LoDs of 9 and 13 fM, respectively (Extended Data Fig. 4, Supplementary Fig. 3 and Supplementary Table 2). Collectively, combining with reporters with extended length (≥11 nucleotides), RBD#3L and #4L exhibited a constantly enhanced collateral activity relative to the WT under all tested conditions.

Characterization of RBD#3L and RBD#4L. To systematically evaluate the collateral activity of RBD#3L and #4L, we performed an unbiased test using 11 crRNAs tiled along the length of a ssRNA1 target[4] (Fig. 4a,b and Supplementary Fig. 4a). RBD#3L and #4L demonstrated enhanced collateral activity at all sites over 120 min, regardless of the spacer sequence (Fig. 4a). Fluorescence signals produced by the two RBD fusions at an early point (30 min) ranged from 2.6- to 13.4-fold higher than the WT signal, with an average of 5.3-fold increase (Fig. 4b), indicating an accelerated reaction rate with all tested spacers. These results demonstrated that RBD#3L and #4L have enhanced collateral activity while retaining programmability.

To test if the target recognition specificity could be affected by the enhanced collateral activity of RBD#3L and #4L, we introduced single mutations (MMs) at every two nucleotides, or consecutive double mutations (DMs) at every four nucleotides across a 28-nucleotide synthetic SARS-CoV-2 N gene target (Supplementary Fig. 4b). Comparison of the relative fold change in background-subtracted fluorescence produced upon incubation with each mismatched target versus that of the perfect-match (PM) target revealed no significant difference in the normalized fluorescence signal, indicating that RBD#3L and #4L maintain the specificity of the WT LwaCas13a (Fig. 4c). Collectively, our data demonstrated that RBD#3L and #4L enhance collateral activity in a spacer-independent manner without compromising the intrinsic programmability and targeting specificity of LwaCas13a, suggesting that these two fusion proteins can be widely used for RNA detection.

To further characterize RBD#3L and #4L, we measured their RNA binding affinity (K_D) and catalytic efficiency (k_{cat}/K_M) in comparison with the WT. Electrophoretic mobility shift assays showed K_D values of 23, 18, and 46 nM using a 36-nucleotide target RNA binding with the complex of the catalytically inactive HEPN2 domain mutants (R1046A/H1051A), that is, dRBD#3L, dRBD#4L and dWT, and the crRNA (Extended Data Fig. 5a,b). By using a longer target (105 nucleotides), K_D values were measured as 12, 11, and 16 nM for dRBD#3L, dRBD#4L, and dWT RNPs, respectively (Extended Data Fig. 5c,d), again showing a higher target RNA binding affinity of the RBD fusions than the WT. In addition to the enhanced target binding, the reporter binding affinity was also improved by RBD fusions. The estimated K_D values were ~0.23, 0.15, and 0.47 μM for U_{20} reporter binding with dRBD#3L, dRBD#4L, and dWT, respectively (Extended Data Fig. 5e–g and Supplementary Table 3). In agreement with the K_D of reporter–protein binding, the Michaelis–Menten collateral cleavage kinetics using U_{11} as the substrate showing K_M values were 1.9, 0.48, and 7 μM and the catalytic efficiency (k_{cat}/K_M) of reporter cleavage was 1.7×10^7, 1.5×10^7, and 3.9×10^6 $M^{-1}s^{-1}$ for RBD#3L, RBD#4L, and the WT, respectively (Extended Data Fig. 6 and Supplementary Table 4). The catalytic efficiency of RBD#3L and RBD#4L remained two- to threefold higher than that of the WT in reactions using reaction buffer supplemented with 0.01% bovine serum albumin and Triton X-100 (Supplementary Fig. 5). Taken together, RBD#3L and #4L exhibited increased binding affinities to both target and reporter RNAs, as well as improved collateral cleavage efficiency.

Detect various targets using Cas13a variants. To evaluate the broader application of these LwaCas13a variants, we used both RBD#3L and #4L to detect a variety of clinically relevant RNA targets, including RNA targets from SARS-CoV-2, Zika, Dengue,

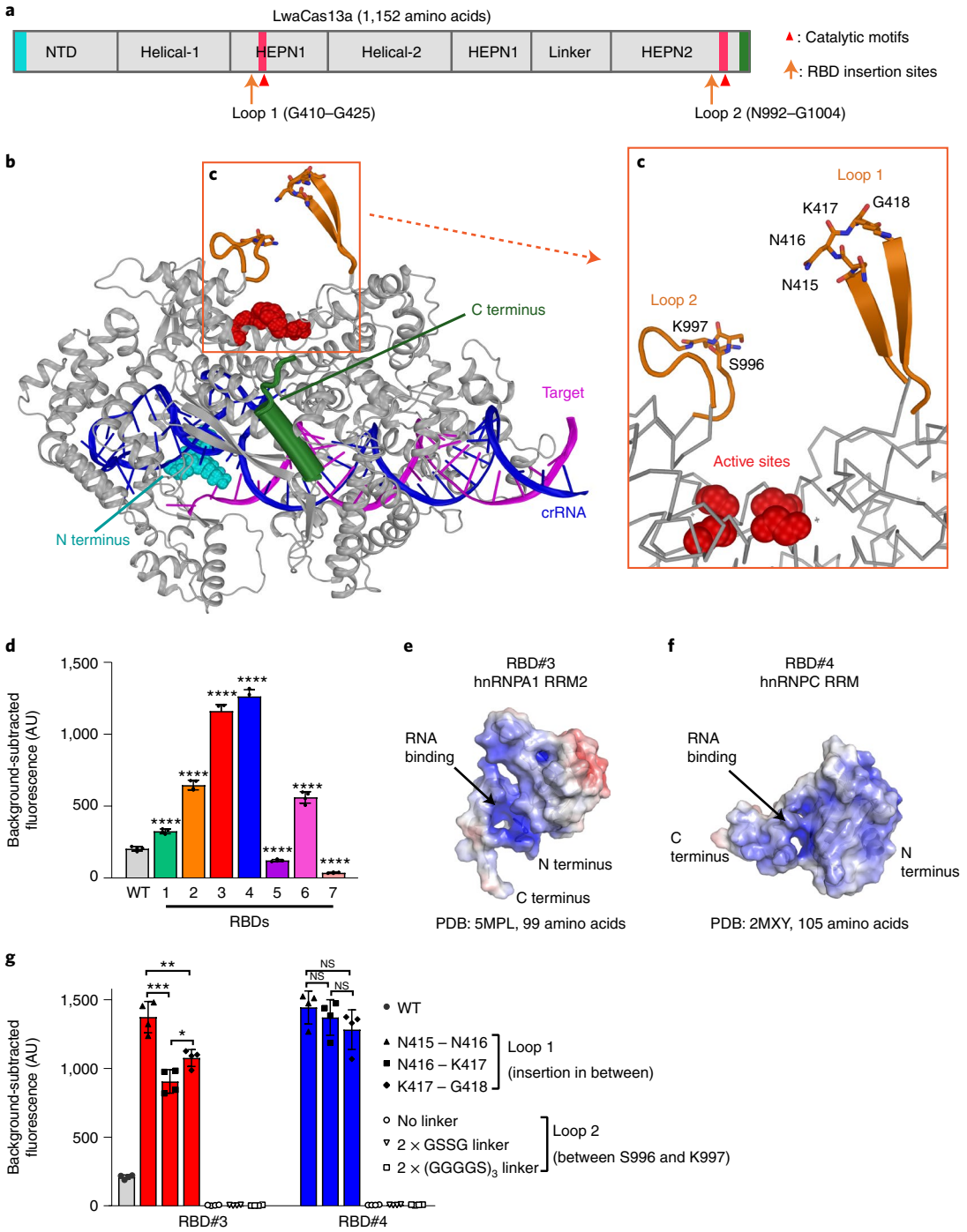

Fig. 2 | Structure-guided design of RBD–LwaCas13a fusion proteins with enhanced collateral activity. a, Domain organization of LwaCas13a by alignment to LbuCas13a (PDB ID: 5XWP). N- and C-terminal ends are labeled cyan and green, respectively. Catalytic motifs, R474–H479 in HEPN1 and R1046–H1051 in HEPN2 are labeled red. Loop regions for RBD insertion, G410–G425 (denoted as Loop 1) and N992–G1004 (denoted as Loop 2), are labeled orange. NTD, N-terminal domain. **b**, Ribbon representation of the predicted structure of LwaCas13a (gray)–crRNA (blue)–target RNA (purple) ternary complex. The N terminus is labeled cyan and the C terminus is labeled green. The four catalytic residues, R474, H479, R1046, and H1051 are labeled red. Loop 1 and Loop 2 are labeled orange. **c**, An expanded view of the catalytic residues and two active-site-proximal loops. Loop-fusion proteins were constructed by inserting RBDs between indicated residues, including N415, N416, K417, and G418, or S996 and K997. **d**, Background-subtracted fluorescence comparing the collateral activity between WT and seven Loop 1 fusions (RBD#1L–#7L, in which RBDs were inserted between N415 and N416 in Loop 1). **e**,**f**, Surface views of RBD#3 (**e**), that is, hnRNP A1 RRM2 (PDB ID: 5MPL), and RBD#4 (**f**), that is, hnRNP C RRM (PDB ID: 2MXY). N and C termini, and RNA-binding regions for both RBDs are labeled. **g**, Background-subtracted fluorescence showing the collateral activity of WT, RBD#3, and RBD#4 loop-fusion variants. Six constructs for each RBD were tested, including three Loop 1 variants with RBD directly inserted between N415 and N416, between N416 and K417, or between N417 and G418, and three Loop 2 variants with RBD inserted between S996 and K997, including direct insertion with no linker, with flanking GSSG linker, or $(GGGGS)_3$ linker, respectively. For **d**,**g**, 10 pM of synthetic RNA (T1) was detected by WT and loop-fusion variants. The bar plot represented the 30-min background-subtracted fluorescence expressed as mean ± s.e.m. from four technical replicates. Two-tailed *P* values were calculated using unpaired *t*-tests: $^{*}P = 0.0177$; $^{**}P = 0.0037$, $^{***}P = 0.0006$, $^{****}P < 0.0001$ (see Source Data for *P* values).

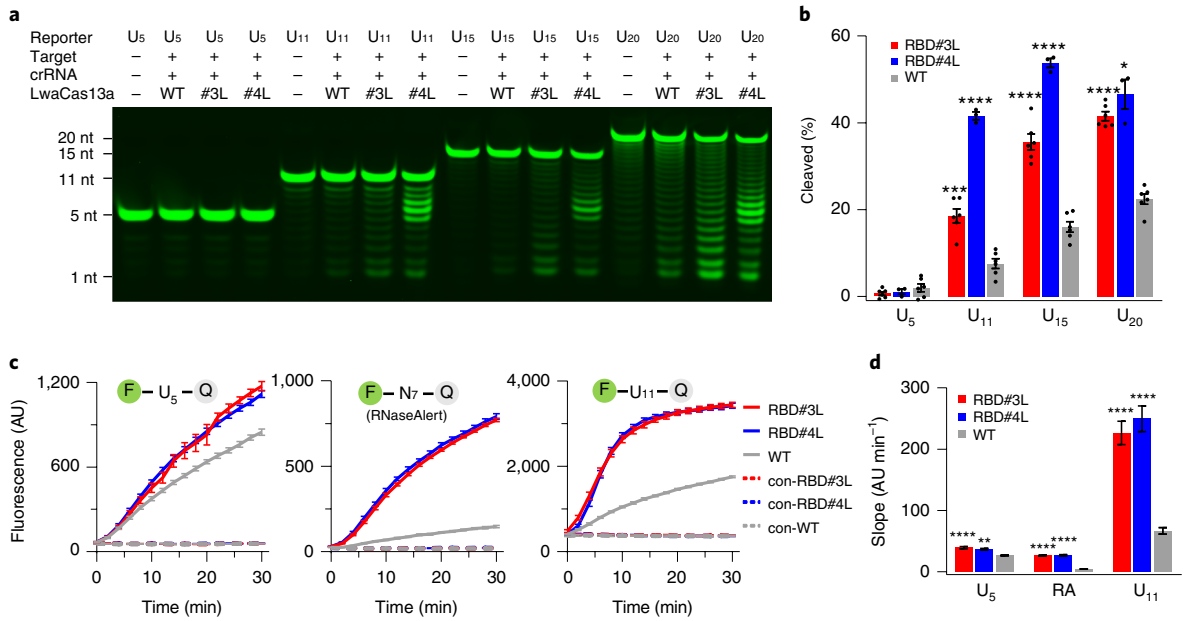

Fig. 3 | Optimizing reporter length for enhanced collateral activity. a, Representative gel of the cleavage of 5′-FAM-labeled U_5, U_{11}, U_{15}, and U_{20} reporters by the WT LwaCas13a, RBD #3L, and RBD#4L after a 10-min incubation. nt, nucleotides **b**, Quantified percentage of cleaved products as shown in **a**, represented by mean ± s.e.m. of six replicates from two independent experiments each with three technical replicates for WT and RBD#3L, and of three technical replicates for RBD#4L. Gels were analyzed by ImageJ. The percentage of cleaved products was calculated by the intensity of product bands divided by the summed intensity of the product and substrate bands within one lane and normalized to the reporter-only control. Two-tailed *P* values were calculated using unpaired *t*-tests with Welch's correction: $^*P = 0.0116$; $^{***}P = 0.0004$; $^{****}P < 0.0001$; compared to WT (see Source Data for *P* values). **c**, Time course of raw fluorescence generated by cleavage of RNaseAlert (IDT), fluorophore–quencher pairs connected by U_5 or U_{11}. Reporters were incubated with WT, RBD#3L, or #4L with the presence or absence of 10 pM of the T1 targets. Controls were reactions in the absence of a target (con-RBD#3L, con-RBD#4L, and con-WT). Data are represented as mean ± s.e.m. The error bar is shown from four technical replicates. **d**, Mean slope ± 95% confidence interval (95% CI) was calculated from **c**; fluorescence signal over 30 min for U_5 and RNaseAlert (RA), and over 10 min for U_{11} by simple linear regression. Adjusted *P* values were calculated using two-way ANOVA with Dunnett's test: $^{**}P = 0.011$; $^{****}P < 0.0001$; compared to WT (see Source Data for adjusted *P* value).

Ebola viruses, and two short microRNA (miR) targets, miR-19b as a predictive biomarker for cardiovascular death[29] and miR-2392 as a diagnostic marker for COVID-19 severity[30]. The matrices and contaminants from biofluids usually reduce the sensitivity of a CRISPR-based detection[3,14,28]. To mimic a direct detection of RNA targets from the complex composition of their diagnostic samples[29–35], we spiked these synthetic RNA targets into the corresponding biological specimen types containing background RNAs. Before the fluorescence plate reader assay, biofluid samples were treated with the HUDSON methods[28,36–38] to simulate the release of RNA from viral particles or exosomes and eliminate the nuclease activity from the samples.

In detecting the SARS-CoV-2 N gene target, with the addition of 8% viral transportation medium (VTM) or 8% saliva to the reaction buffer alone, the WT showed 40% decreased activity, while RBD#3L demonstrated comparable or slightly increased activity and RBD#4L exhibited 2.6- or 2.2-fold increased activity (Fig. 5a and Extended Data Fig. 7a,b). Detecting the same target in reactions containing 16% VTM, RBD#3L retained 78% of the signal, however, only 30% signal remained in WT, compared to reactions with buffer alone (Extended Data Fig. 8a). Using similar approaches, Zika, Dengue, and Ebola virus RNA targets were detected in reactions containing 8% urine, 2.5% serum, or 2.5% plasma, respectively. The WT showed as much as 68% reduced signal in the presence of those complex matrices (Fig. 5b–d and Extended Data Fig. 7c–e), while RBD#3L and #4L retained good activity and showed 2.5- to 6.7-fold signals relative to the WT. When higher concentrations of these matrices were used (that is, 16% urine, 4.8% serum, and 4.8% plasma), RBD#3L still retained 43%, 78%, and 93% of the signal compared to those reactions in buffer-only conditions (Extended Data Fig. 8b–d). Likewise, RBD#3L and RBD#4L collateral activity in response to a 23-nucleotide miR-19b target were 4.7- and 7.3-fold relative to WT in reactions containing 2.5% serum or 2.5% plasma (Fig. 5e and Extended Data Fig. 7f,g). Finally, RBD#4L showed 28- and 14-fold activities relative to WT in detecting a 20-nucleotide miR-2392 (discovered only in serum and urine[30]) from samples containing 2.5% serum and 8% urine, respectively (Fig. 5f and Extended Data Fig. 7h–j). Collectively, RBD#3L and #4L showed enhanced collateral cleavage over the WT in various buffer conditions (Fig. 5, Extended Data Figs 7 and 8, and Supplementary Figs 1 and 2). In complex reaction conditions, such as the biofluid-containing samples, we observed RBD#4L maintained more robust collateral activity than RBD#3L (Fig. 5 and Extended Data Figs 7 and 8), suggesting that the intrinsic RBD#4–PolyU binding affinity[23] facilitates effective collateral cleavage (Supplementary Fig. 6). Our results showed that RBD#3L and #4L exhibited superior robustness in detecting target RNAs from biofluid-containing samples, holding great potential for field-deployable detection of various RNAs for diagnostic purposes.

Ultrasensitive and amplification-free RNA detection. To demonstrate RBD#3L and #4L could be employed for on-site diagnosis of virus infection, we integrated their target-activated collateral cleavage reaction into a screen-printed electrode (SPE) device (Supplementary Fig. 7). The working electrode (WE) of this device was first functionalized with the U_{20} tagged with methylene blue (MB), a redox-active electrochemical reporter, the surface density of which was estimated to be ~25 pmol mm^{-2} (Supplementary Fig. 8). The electron transfer between the WE and redox-active MB

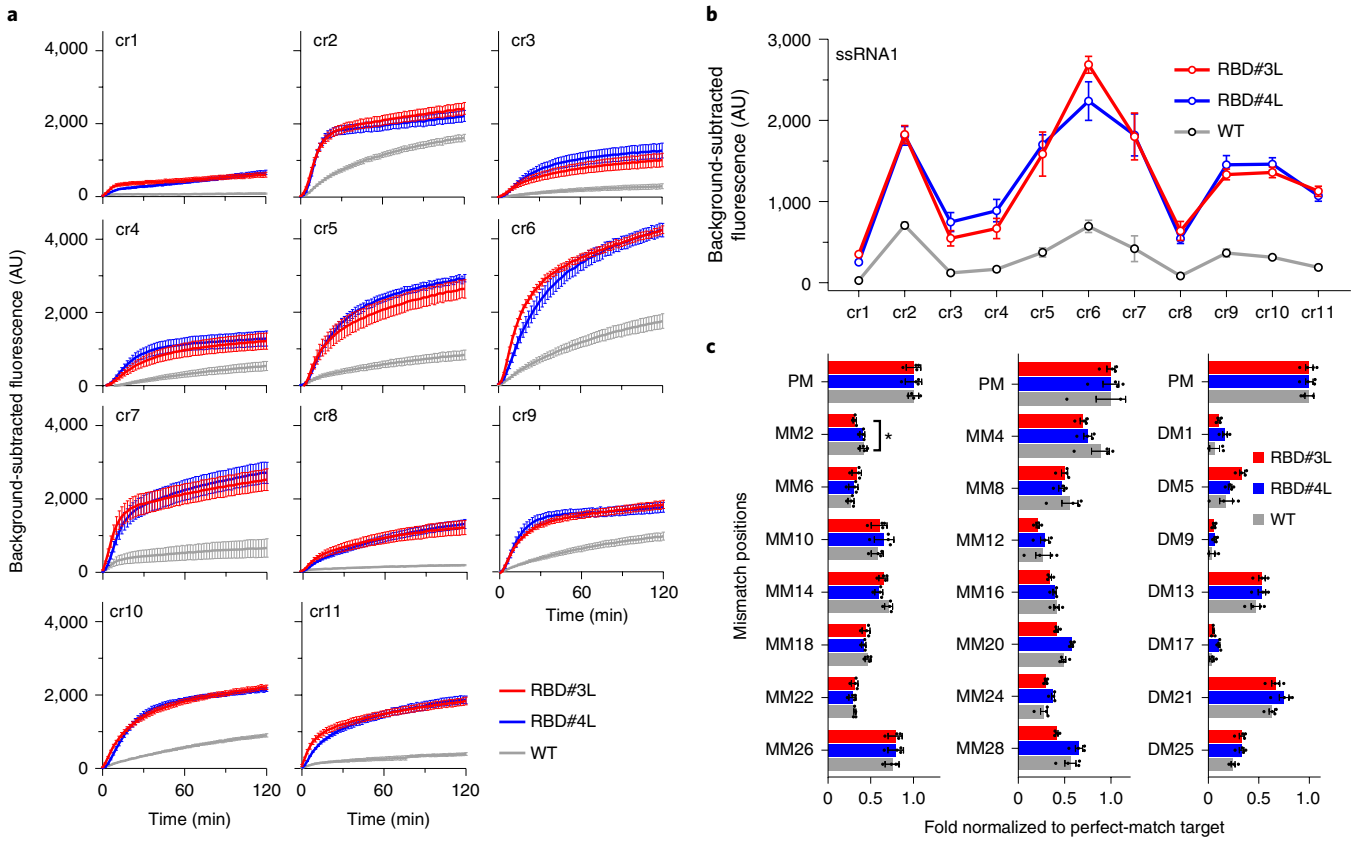

Fig. 4 | RBD#3L and #4L enhance the collateral activity in a spacer-independent manner and maintain the specificity for target recognition. **a**, Background-subtracted fluorescence over 120 min comparing the collateral activity of WT, RBD#3L, and RBD#4L with 11 crRNAs (cr4–cr14) evenly tiled across ssRNA1 target (T3). Data are represented as mean ± s.e.m. from four technical replicates. **b**, Background-subtracted fluorescence early point (30 min) from **a**, showing increased collateral cleavage by RBD#3L and #4L. **c**, Single-point mutations (left: MM2, MM6, MM10, MM14, MM18, MM22, and MM26; middle: MM4, MM8, MM12, MM16, MM20, MM24, and MM28); and double-point mutations (right: DM1, DM5, DM9, DM13, DM17, DM21, and DM25) were introduced to the 28-nucleotide RNA target (T5–T25). Bar graphs are mean ± s.e.m. from four technical replicates, indicating the normalized fold change of background-subtracted fluorescence of point mutation to the corresponding perfectly matched (PM) target (T4). Adjusted *P* values were calculated using Holm–Sidak multiple *t*-tests. Unless indicated, no significant difference was observed from each point mutation, that is, RBD#3L versus WT and RBD#4L versus WT. *$P = 0.03498$, compared to WT LwaCas13a (see Source Data for adjusted *P* value).

was acquired by square wave voltammetry (SWV)[39]. Cleavage of MB-tagged U_{20} reporters from the WE by Cas13a collateral activity is triggered by recognition of an RNA target and results in a decrease in the peak electrochemical current expressed by ΔI% (Supplementary Fig. 7). Evaluation of the analytical performance of the endpoint Cas13–electrochemical assay using serial dilutions of a synthetic SARS-CoV-2 N gene target (1 aM to 100 pM in the reaction) revealed an estimated LoD of 1 pM (two-tailed $P = 0.0109$, unpaired *t*-test with Welch's correction) for WT LwaCas13a (Fig. 6a and Extended Data Fig. 9a). By using RBD#3L and RBD#4L, the LoD of this system was dramatically improved to 10 aM (Fig. 6b,c and Extended Data Fig. 9b,c). Further measurement of the time-course electrochemical signals every 30 s by repeated SWV scans (Methods; Supplementary Fig. 8) and demonstrated clear discrimination of the reactions containing 10 aM targets from the non-target control by using RBD#3L and #4L, while the WT showed only background-level signal (Supplementary Fig. 9). The best-fit pseudo-first-order rate constants (that is, observed rate constant, k_{obs}) at a target concentration of 10 aM were 0.007356 s^{-1}, 0.003639 s^{-1}, and 1.213×10^{-8} s^{-1} for RBD#3L, #4L, and the WT, respectively, showing over 10^5-fold improvement of the k_{obs} upon RBD fusion.

To test the efficacy of this system for detection of genomic RNA, the heat-inactivated SARS-CoV-2 samples from infected Vero E6 cells were treated with a 5-min extraction-free procedure[40] and analyzed. The WT-based system could not distinguish between the virus stock sample with the highest viral RNA concentration (16.2 fM in the reaction) and the blank (non-target control with water input undergone the same treatment as the samples) (Fig. 6d). Notably, an RBD#3L-based system detected a significant difference ($P = 0.0343$) between the blank and 1 aM (final concentration in the reaction) viral RNA (Fig. 6e). Similar results were observed when the RBD#4L was used in place of RBD#3L in this system, with a significant difference ($P = 0.0274$) observed between the blank and 1 aM target reactions (Fig. 6f).

Finally, we compared the performance of the WT, RBD#3L, and RBD#4L systems in detecting clinical SARS-CoV-2 samples (Fig. 6g–i). The VTM leftovers for storage of the nasopharyngeal swab biospecimens were all heat-inactivated and labeled as SARS-CoV-2 positive or negative on the basis of the PCR or isothermal nucleic acid amplification tests used at UConn Health for diagnostic purposes. We first quantified the specific viral loads by performing quantitative PCR with reverse transcription (RT–qPCR) using purified RNA from these clinical samples (Supplementary Fig. 10). Eleven samples were confirmed positive with C_q values ranging from 34 to 22, equivalent to a viral load from 1.9 to 32,066 copies per microliter (3 aM to 53 fM) in electrochemical assay (Supplementary Table 5) and ten samples

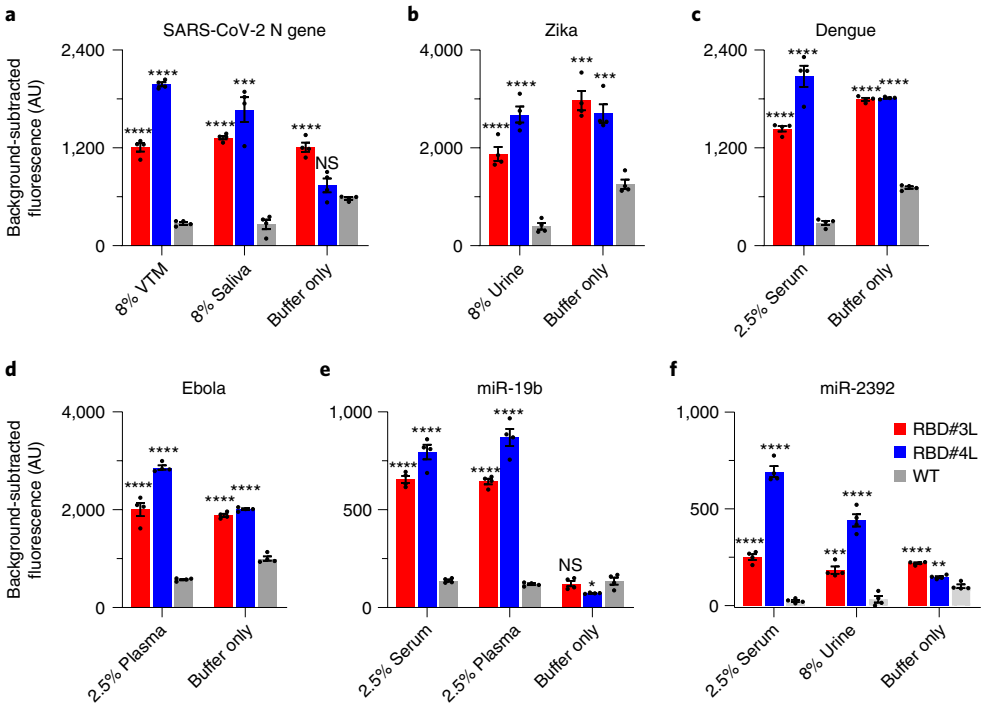

Fig. 5 | Improved detection of various spiked-in targets. a–f, Background-subtracted fluorescence in the detection of 10 pM of: SARS-CoV-2 N gene synthetic targets (T1) spiked into 8% VTM, 8% saliva, or reaction buffer (**a**); Zika synthetic targets (T27) spiked into 8% urine, or reaction buffer (**b**); Dengue synthetic targets (T28) spiked into 2.5% serum or reaction buffer (**c**); Ebola (T29) synthetic targets spiked into 2.5% plasma, or reaction buffer (**d**); miR-19b (T30) spiked into 2.5% serum, 2.5% plasma, or reaction buffer (**e**); and 200 pM of miR-2392 (T31) spiked into 2.5% serum, 8% urine, or reaction buffer (**f**). All reactions were supplemented with 50 ng total RNA extracted from HEK293T cells. Bar graphs are the 30-min background-subtracted fluorescence mean ± s.e.m. from four technical replicates. Two-tailed *P* values were calculated using unpaired *t*-tests: $^{*}P < 0.05$; $^{**}P < 0.01$; $^{***}P < 0.001$; and $^{****}P < 0.0001$; compared to the corresponding WT under the same testing conditions. More specifically: **a**, $^{***}P = 0.0001$; **b**, $^{***}P = 0.0002$ for RBD#3L and 0.0005 for RBD#4L; **e**, $^{*}P = 0.0140$; **f**, $^{***}P = 0.001$, $^{**}P = 0.0045$ (see Source Data for *P* values).

were determined to be negative. The raw samples were subjected to 5-min quick treatment at 95 °C to eliminate nuclease activity and facilitate viral RNA release and tested using an electrochemical sensor coupled with the WT, RBD#3L, and RBD#4L, respectively (Fig. 6g–i). A detection threshold was set to two standard deviations above the mean of blank samples[17] (non-target control reactions with empty VTM in place of clinical samples), allowing distribution of more than ~95% of the clinical negative samples below the detection criteria. Following this standard, RBD#3L detected nine and RBD#4L detected ten positive samples within 30 min (Fig. 6h,i and Supplementary Table 5). One positive sample (P11) with a C_q value of 34 (1.9 copies per microliter in the electrochemical assay) could not be detected by both RBD#3L and #4L, while P9 with a C_q value of 32 (12 copies per microliter) could be successfully detected by RBD#4L. When ten negative samples were tested by using either RBD#3L or #4L, no false-positive data was shown in our analysis, showing the high accuracy of our method. Notably, the WT LwaCas13a cannot detect the positive samples with the highest available concentrations (P2, P4, and P8 with C_q values of 22, 22, and 26, respectively; Fig. 6g and Supplementary Table 5). We attribute the remarkably improved sensitivity of RBD#3L and #4L compared to WT on the electrochemical biosensor to a synergistic effect of several factors, including the enhanced reporter RNA binding with the RBD proximal to the active site of LwaCas13a and the surface chemistry at the reaction interface. On the basis of these findings we believe that RBD–LwaCas13a proteins engineered with improved collateral activity can be integrated into diverse detection platforms to detect pathogen- or host-derived RNA targets in the clinical laboratory or point-of-care settings.

Discussion

In this study, we demonstrated that the collateral activity of WT LwaCas13a can be improved by structure-guided protein engineering. We generated LwaCas13a variants with enhanced collateral activity by inserting selected RBDs to the tip of an active-site-proximal loop. Two of the most potent variants, RBD#3L and #4L, increased the collateral cleavage rates in various buffer conditions. When further integrated with an electrochemical device, these two variants detected attomolar levels of viral RNA targets without preamplification. Our engineered protein with increased collateral activity also showed high accuracy in analyzing clinical SARS-CoV-2 samples and can detect positive samples with a concentration as low as 12 copies per microliter (final concentration in the electrochemical assay). Our technology utilizes an engineered LwaCas13a enzyme to increase the collateral activity and therefore can be readily integrated into a variety of previously established Cas13a-based detection platforms[4,6,13,14,28].

Since the emergence of CRISPR-based technologies for the detection of nucleic acids, many attempts have improved reaction sensitivity for fast on-site detection of nucleic acids using a variety of approaches including target preamplification[3,4], auxiliary proteins with corresponding activator RNA additions[4,22], multiple crRNA combinations[16], reaction optimization[28], field-deployable sample treatment[36], and versatile sensing devices[14,16–18,39]. However, it has been challenging to engineer the Cas13a protein owing to its structural complexity and catalytic dynamics as an active RNase. Reported studies on Cas13 protein engineering were exclusively for in vivo editing or targeting of RNAs[41–44]. Among those studies, the design of a Cas13 fusion protein has followed the established strategy of tethering functional proteins or domains to the N and/

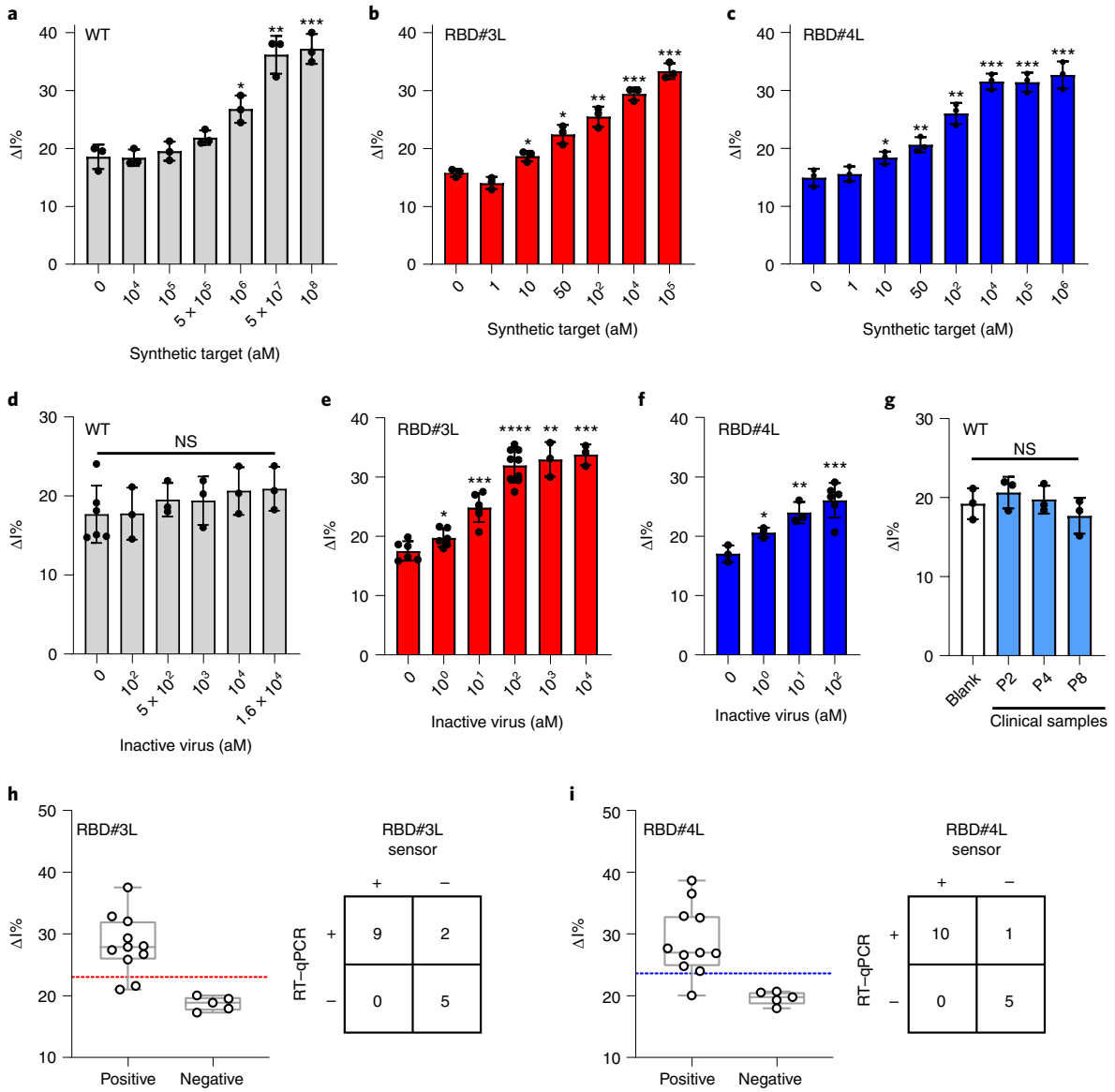

Fig. 6 | RBD fusions facilitate electrochemical detection of RNA at attomolar sensitivity. a–c, Electrochemical detection of synthetic RNA target. WT (**a**), RBD#3L (**b**), or RBD#4L (**c**) RNPs were activated with various concentrations of the synthetic SARS-CoV-2 N gene target (T1). Blank samples are RNPs without the target. **d–f**, Electrochemical detection of inactive virus RNA. WT (**d**), RBD#3L (**e**), or RBD#4L (**f**) RNPs were activated by serial dilution of the inactive SARS-CoV-2 viral genome. Blank samples are RNPs without the target ($n = 6$ for the 0 aM sample from **d**, 0, 10^0 and 10^1 aM from **e**, and 10^2 aM from **f**; $n = 9$ for 10^2 aM from **e**). **g–i**, Electrochemical detection of SARS-CoV-2 RNA from unextracted raw clinical VTM samples. VTM were leftovers for nasopharyngeal swab storage, and the viral load was quantified by RT-qPCR with standard curve analysis using purified RNA. WT (**g**) was tested with three positive samples (P2, P4, and P8); RBD#3L **(h)** was tested with five negative samples (N1–N5) and 11 positive samples (P1–P11); and RBD#4L (**i**) was tested with five negative samples (N6–N10) and 11 positive samples (P1–P11). Clinical samples were subjected to extraction-free 5-min quick treatment before adding to the reactions. Blank samples were tested in parallel with clinical samples and used VTM as input. **h**,**i**, Box plots with the 25th and the 75th percentile boundaries and the whiskers indicating the minimum, maximum, and mean values of electrochemical signal change (ΔI%) of clinical samples each from three technical replicates. Dotted lines indicate the threshold for electrochemical sensor detection and were set to mean + 2 × s.d. of the blank. Concordance tables between RBD#3L/RBD#4L-sensor and RT-qPCR for clinical samples are shown. For **a–g**, bar plots represented mean ± s.d. of the ΔI% from three technical replicates unless otherwise indicated. Two-tailed *P* values were calculated using unpaired *t*-tests with Welch's correction. Unless indicated, no significant change was observed compared to the corresponding no-target blank sample. $^*P < 0.05$, $^{**}P < 0.01$, $^{***}P < 0.001$, $^{****}P < 0.0001$. More specifically: **a**, $^*P = 0.0109$, $^{**}P = 0.0027$, $^{***}P = 0.0008$; **b**, $^*P = 0.0139$ for 10^1 and $^*P = 0.0103$ for 5×10^1 aM target samples, $^{**}P = 0.0048$, $^{***}P = 0.0002$ and 0.0003 for 10^4 and 10^5 aM target samples; **c**, $^*P = 0.0366$, $^{**}P = 0.0081$ and 0.0015 for 5×10^1 and 10^2 aM target samples, $^{***}P = 0.0001$, 0.0002 and 0.0009 for 10^4, 10^5, and 10^6 aM target samples; **e**, $^*P = 0.0343$, $^{**}P = 0.0053$, $^{***}P = 0.0002$ for both 10^1 and 10^4 aM target samples; **f**, $^*P = 0.0274$, $^{**}P = 0.0073$, $^{***}P = 0.0004$ (see Source Data for *P* values).

or C terminus of a Cas effector[42–44]. We found, however, that the LwaCas13a terminus can be buried (Fig. 2b), and linking additional functional domains/motifs to these termini can lead to a detrimental effect on Cas13a collateral activity. Intriguingly, we identified a β-hairpin loop proximal to its active site that served as a hotspot for Cas13 engineering, since fusing selected RBDs into this loop enhanced RNA binding and cleavage, as well as enzyme stability. A few studies have employed a domain-insertional strategy to add

new functionalities to Cas9, such as inserting a ligand-binding domain for the allosteric regulation[45] or a deaminase to broaden the activity window of base editors[46]; however, these studies did not show enhancement of activity or substrate binding affinity of Cas9[45,46]. Our strategy exploited the RNA binding affinity of selected RRMs and structure-guided domain insertion to dramatically enhance collateral activity while maintaining the programmability and specificity for the target RNA.

There are a large number of known RBDs, including RRMs, DRBMs, and zinc-finger RNA domains, which interact with RNA in a non-sequence-specific manner, especially under physiological conditions where interacting RNAs are present at low abundance[20,47,48]. Further exploration of the RBD repertoire may lead to the discovery of more active and robust Cas13a variants. In addition to diagnostic context, these engineered Cas13a proteins could potentially be used for the detection of agricultural pathogens and sensing of proteins and small molecules when in combination with other biotechnologies. Our case study on LwaCas13a points to a new direction for future engineering studies on other Cas enzymes, which are usually large and may contain other potential structural loops proximal to their active sites for fusing other regulatory/functional domains for both in vitro and in vivo applications.

Notably, the inclusion of our engineered RBD–LwaCas13a fusion proteins into a U_{20} RNA redox-reporter-functionalized SPE device enabled the detection of heat-inactivated SARS-CoV-2 viral genome at attomolar sensitivity and successfully identified the unextracted clinical SARS-CoV-2 positive samples, without target preamplification. Our engineered CRISPR–Cas system is among one of the most sensitive CRISPR-based amplification-free technologies for the detection of nucleic acid developed to date in detecting the SARS-CoV-2 genome (LoD 0.6 copies per microliter in the reaction, within 30 min). It shows comparable sensitivity to the droplet-based Cas13a kinetic barcoding (below 1 copy per microliter), which contained a total of 26 crRNAs in one single assay[49]; it is one order of magnitude more sensitive than that of the Cas13a–Csm6 tandem assay (31 copies per microliter), which required eight different crRNAs and a Csm6 protein with its chemically modified activator RNA[17]; two orders of magnitude more sensitive than the Cas13a–mobile phone microscopy (200 copies per microliter), which utilized three different crRNAs[16]; three orders of magnitude more sensitive than the Cas13–microchamber array[14], and six orders of magnitude more sensitive than the CRISPR–electrochemical biosensor that depends on the WT Cas13a protein[18]. As opposed to the aforementioned amplification-free detection technologies that are exclusively based on extracted RNA materials, our RBD–LwaCas13a–electrochemistry platform showed great detection sensitivity and accuracy and does not need the additional RNA extraction steps, which holds great potential for ultrasensitive detection of various RNAs of clinical and environmental importance.

Online content

Any methods, additional references, Nature Research reporting summaries, source data, extended data, supplementary information, acknowledgements, peer review information; details of author contributions and competing interests; and statements of data and code availability are available at https://doi.org/10.1038/s41589-022-01135-y.

Received: 19 October 2021; Accepted: 8 August 2022;
Published online: 22 September 2022

References

1. Shmakov, S. et al. Discovery and functional characterization of diverse Class 2 CRISPR–Cas systems. *Mol. Cell* **60**, 385–397 (2015).
2. Liu, L. et al. The molecular architecture for RNA-guided RNA cleavage by Cas13a. *Cell* **170**, 714–726.e10 (2017).
3. Gootenberg, J. S. et al. Nucleic acid detection with CRISPR–Cas13a/C2c2. *Science* **356**, 438–442 (2017).
4. Gootenberg, J. S. et al. Multiplexed and portable nucleic acid detection platform with Cas13, Cas12a, and Csm6. *Science* **360**, 439–444 (2018).
5. Qin, P. et al. Rapid and fully microfluidic Ebola virus detection with CRISPR–Cas13a. *ACS Sens.* **4**, 1048–1054 (2019).
6. Ackerman, C. M. et al. Massively multiplexed nucleic acid detection with Cas13. *Nature* **582**, 277–282 (2020).
7. Patchsung, M. et al. Clinical validation of a Cas13-based assay for the detection of SARS-CoV-2 RNA. *Nat. Biomed. Eng.* **4**, 1140–1149 (2020).
8. Kaminski, M. M., Abudayyeh, O. O., Gootenberg, J. S., Zhang, F. & Collins, J. J. CRISPR-based diagnostics. *Nat. Biomed. Eng.* **5**, 643–656 (2021).
9. Kellner, M. J., Koob, J. G., Gootenberg, J. S., Abudayyeh, O. O. & Zhang, F. SHERLOCK: nucleic acid detection with CRISPR nucleases. *Nat. Protoc.* **14**, 2986–3012 (2019).
10. Zou, Y., Mason, M. G. & Botella, J. R. Evaluation and improvement of isothermal amplification methods for point-of-need plant disease diagnostics. *PLoS ONE* **15**, e0235216 (2020).
11. Hardinge, P. & Murray, J. A. H. Reduced false positives and improved reporting of loop-mediated isothermal amplification using quenched fluorescent primers. *Sci. Rep.* **9**, 7400 (2019).
12. Khan, P., Aufdembrink, L. M. & Engelhart, A. E. Isothermal SARS-CoV-2 diagnostics: tools for enabling distributed pandemic testing as a means of supporting safe reopenings. *ACS Synth. Biol.* **9**, 2861–2880 (2020).
13. Bruch, R. et al. CRISPR-powered electrochemical microfluidic multiplexed biosensor for target amplification-free miRNA diagnostics. *Biosens. Bioelectron.* **177**, 112887 (2021).
14. Shinoda, H. et al. Amplification-free RNA detection with CRISPR–Cas13. *Commun. Biol.* **4**, 476 (2021).
15. Arnaout, R. et al. The limit of detection matters: the case for benchmarking severe acute respiratory syndrome coronavirus 2 testing. *Clin. Infect. Dis.* **73**, e3042–e3046 (2021).
16. Fozouni, P. et al. Amplification-free detection of SARS-CoV-2 with CRISPR–Cas13a and mobile phone microscopy. *Cell* **184**, 323–333.e9 (2021).
17. Liu, T. Y. et al. Accelerated RNA detection using tandem CRISPR nucleases. *Nat. Chem. Biol.* **17**, 982–988 (2021).
18. Bruch, R. et al. CRISPR/Cas13a-powered electrochemical microfluidic biosensor for nucleic acid amplification-free miRNA diagnostics. *Adv. Mater.* **31**, e1905311 (2019).
19. Lunde, B. M., Moore, C. & Varani, G. RNA-binding proteins: modular design for efficient function. *Nat. Rev. Mol. Cell Biol.* **8**, 479–490 (2007).
20. Hentze, M. W., Castello, A., Schwarzl, T. & Preiss, T. A brave new world of RNA-binding proteins. *Nat. Rev. Mol. Cell Biol.* **19**, 327–341 (2018).
21. Bass, B. L. RNA editing by adenosine deaminases that act on RNA. *Annu. Rev. Biochem.* **71**, 817–846 (2002).
22. Beusch, I., Barraud, P., Moursy, A., Clery, A. & Allain, F. H. Tandem hnRNP A1 RNA recognition motifs act in concert to repress the splicing of survival motor neuron exon 7. *Elife* **6**, e25736 (2017).
23. Cieniková, Z., Damberger, F. F., Hall, J., Allain, F. H. T. & Maris, C. Structural and mechanistic insights into poly(uridine) tract recognition by the hnRNP C RNA recognition motif. *J. Am. Chem. Soc.* **136**, 14536–14544 (2014).
24. Huang, J. et al. Solution structure of the RNA recognition domain of METTL3-METTL14 N^6-methyladenosine methyltransferase. *Protein Cell* **10**, 272–284 (2019).
25. Placido, D., Brown, B. A., Lowenhaupt, K., Rich, A. & Athanasiadis, A. A left-handed RNA double helix bound by the Zα domain of the RNA-editing enzyme ADAR1. *Structure* **15**, 395–404 (2007).
26. Athanasiadis, A. et al. The crystal structure of the Zβ domain of the RNA-editing enzyme ADAR1 reveals distinct conserved surfaces among Z-domains. *J. Mol. Biol.* **351**, 496–507 (2005).
27. Baek, M. et al. Accurate prediction of protein structures and interactions using a three-track neural network. *Science* **373**, 871–876 (2021).
28. Arizti-Sanz, J. et al. Streamlined inactivation, amplification, and Cas13-based detection of SARS-CoV-2. *Nat. Commun.* **11**, 5921 (2020).
29. Karakas, M. et al. Circulating microRNAs strongly predict cardiovascular death in patients with coronary artery disease-results from the large AtheroGene study. *Eur. Heart J.* **38**, 516–523 (2017).
30. McDonald, J. T. et al. Role of miR-2392 in driving SARS-CoV-2 infection. *Cell Rep.* **37**, 109839 (2021).
31. Santiago, G. A. et al. Analytical and clinical performance of the CDC real time RT–PCR assay for detection and typing of Dengue virus. *PLoS Negl. Trop. Dis.* **7**, e2311 (2013).
32. Broadhurst, M. J., Brooks, T. J. & Pollock, N. R. Diagnosis of Ebola virus disease: past, present, and future. *Clin. Microbiol Rev.* **29**, 773–793 (2016).
33. Byrne, R. L. et al. Saliva alternative to upper respiratory swabs for SARS-CoV-2 diagnosis. *Emerg. Infect. Dis.* **26**, 2770–2771 (2020).

34. Reijns, M. A. M. et al. A sensitive and affordable multiplex RT–qPCR assay for SARS-CoV-2 detection. *PLoS Biol.* **18**, e3001030 (2020).
35. Ning, B. et al. A smartphone-read ultrasensitive and quantitative saliva test for COVID-19. *Sci. Adv.* **7**, eabe3703 (2021).
36. Myhrvold, C. et al. Field-deployable viral diagnostics using CRISPR–Cas13. *Science* **360**, 444–448 (2018).
37. Barnes, K. G. et al. Deployable CRISPR-Cas13a diagnostic tools to detect and report Ebola and Lassa virus cases in real-time. *Nat. Commun.* **11**, 4131 (2020).
38. Shan, Y., Zhou, X., Huang, R. & Xing, D. High-fidelity and rapid quantification of miRNA combining crRNA programmability and CRISPR/Cas13a trans-cleavage activity. *Anal. Chem.* **91**, 5278–5285 (2019).
39. Dai, Y. et al. Exploring the trans-cleavage activity of CRISPR–Cas12a (cpf1) for the development of a universal electrochemical biosensor. *Angew. Chem. Int. Ed. Engl.* **58**, 17399–17405 (2019).
40. Ladha, A., Joung, J., Abudayyeh, O., Gootenberg, J. & Zhang, F. A 5-min RNA preparation method for COVID-19 detection with RT–qPCR. Preprint at *medRxiv* https://doi.org/10.1101/2020.05.07.20055947 (2020).
41. Richter, M. F. et al. Phage-assisted evolution of an adenine base editor with improved Cas domain compatibility and activity. *Nat. Biotechnol.* **38**, 883–891 (2020).
42. Cox, D. B. T. et al. RNA editing with CRISPR–Cas13. *Science* **358**, 1019–1027 (2017).
43. Abudayyeh, O. O. et al. A cytosine deaminase for programmable single-base RNA editing. *Science* **365**, 382–386 (2019).
44. Han, S. et al. RNA–protein interaction mapping via MS2- or Cas13-based APEX targeting. *Proc. Natl Acad. Sci. USA* **117**, 22068–22079 (2020).
45. Oakes, B. L. et al. Profiling of engineering hotspots identifies an allosteric CRISPR–Cas9 switch. *Nat. Biotechnol.* **34**, 646–651 (2016).
46. Chu, S. H. et al. Rationally designed base editors for precise editing of the sickle cell disease mutation. *CRISPR J.* **4**, 169–177 (2021).
47. Jolma, A. et al. Binding specificities of human RNA-binding proteins toward structured and linear RNA sequences. *Genome Res* **30**, 962–973 (2020).
48. Dominguez, D. et al. Sequence, structure, and context preferences of human RNA binding proteins. *Mol. Cell* **70**, 854–867 (2018).
49. Son, S. et al. Sensitive and multiplexed RNA detection with Cas13 droplets and kinetic barcoding. Preprint at *medRxiv* https://doi.org/10.1101/2021.08.02.21261509 (2021).

Methods

Plasmid construct design and molecular cloning. Sequences encoding seven candidate RBDs (Supplementary Table 1) were amplified from HEK293T cDNA. First, total RNA was extracted by Trizol (Invitrogen, 15596026) reagent per the manufacturer's protocols, treated with RNase-free DNase I (New England Biolabs (NEB), M0303S) at 37 °C for 30 min to remove genomic DNA, and heated at 70 °C for 5 min to inactivate DNase activity. To generate cDNA from the RNA extracts, RevertAid First Strand cDNA Synthesis Kit (Thermo Scientific, K1622) was used per the manufacturer's protocols. The RBD-encoding sequences were amplified with Q5 High-Fidelity DNA polymerase (NEB, M0491L) in a 20-µl PCR reaction, comprising 2 µl template cDNA, and 0.5 µM forward and reverse primers (Integrated DNA Technologies (IDT)) with designed 5′ flanking bases and a BsaI restriction site. PCR products were electrophoresed on 1.5% agarose gel with 0.01% (v/v) ethidium bromide in 1× TAE buffer, visualized under a blue-light transilluminator (Accuris) to excise the bands and gel purified (Qiagen, 28076). Cloning primers are listed in Supplementary Note 6.

Purified DNA pieces, RBD alone or RBD with linkers, were Golden-Gate-cloned into an expression vector of LwaCas13a (pC01 3-Twinstrep-SUMO-huLwCas13a; Addgene plasmid #90097), a gift from F. Zhang. A silent mutation was introduced to the vector to eliminate the BsaI restriction site for cloning. N-terminal His-tagged SUMO protease expression plasmid was constructed by amplifying the gene sequence encoding yeast $Ulp1^{403–621}$ from 1 µl *Saccharomyces cerevisiae* strain BY4741 competent cells and Golden Gate cloning into the expression vector of LwaCas13a to replace the twin-strep tag, SUMO tag, and LwaCas13a sequences. The assembled plasmids were transformed to One-Shot Stbl3 Chemically Competent *E. coli* cells (Thermo Scientific, C737303) and grown overnight on a Luria Broth (LB) agar plate containing 100 µg ml^{-1} ampicillin. Colonies containing the correct plasmids, as confirmed by Sanger sequencing (Genewiz), were grown in an ampicillin-supplement LB medium. The plasmids were purified (Qiagen, 27106) and the concentration and purity were measured by a NanoDrop One microvolume Spectrophotometer (Thermo Scientific).

Protein purification. Expression and purification of the WT LwaCas13a and RBD fusion proteins were performed as described in ref. [9] with modifications. In brief, the protein expression vector was transformed into *E. coli* BL21(DE3) competent cells and grown on LB agar plate overnight. A single colony was picked and inoculated in a 5-ml starter culture, grown overnight, and transferred to a flask containing 1 l LB medium. The cultures were grown at 37 °C and 220 r.p.m. until optical density at 600 nm reached 0.4. The cells were cooled on ice for 30 min, induced with 250 µM isopropyl β-D-1-thiogalactopyranoside, and grown for 16 h at 16 °C and 160 r.p.m. Cell pellets were collected by centrifugation at 5,200*g* for 20 min and stored at −80 °C before purification.

All protein purification steps were performed at 4 °C or on ice. The cell pellet was resuspended in lysis buffer (50 mM Tris-HCl, pH 8.0, 1 M NaCl, 10 mM imidazole, 1 mM Tris(2-carboxyethyl) phosphine (TCEP)) supplemented with EDTA-free protease inhibitor tablets (Thermo Scientific, A32965) and mixed by rotation until homogeneous. The cells were then disrupted by sonication (Branson) and the cell lysate was centrifuged at 13,000*g* for 30 min. The supernatant was incubated with Ni-NTA Agarose resin (UBPBio, P3020) and rotated for 30 min. The protein-bound resin was applied to a gravity-flow column for washing and elution. Most of the non-specifically bound proteins were removed by washing buffer 1 (50 mM Tris-HCl, 1 M NaCl, 20 mM Imidazole, 1 mM TCEP, pH 8.0) and 0.5–1 volume of washing buffer 2 (50 mM Tris-HCl, 1 M NaCl, 50 mM Imidazole, 1 mM TCEP, pH 8.0). The protein was eluted using elution buffer (50 mM Tris-HCl, 0.6 M NaCl, 150 mM Imidazole, 1 mM TCEP, pH 8.0). Notably, the TCEP and protease inhibitor was added freshly before use. The SUMO tag was removed by mixing the elute with lab-purified SUMO protease and dialyzed overnight against dialysis buffer (50 mM Tris-HCl, 0.6 M NaCl, 2 mM dithiothreitol (DTT), pH 7.5). The cleaved products were applied to Ni-NTA resins to remove the uncleaved protein and the His-tagged SUMO protease. The collected elute was buffer exchanged to storage buffer (50 mM Tris-HCl, 600 mM NaCl, 5% glycerol, and 2 mM DTT, pH 7.5) and concentrated to ~1.5 mg ml^{-1} using an Amicon Ultra centrifugal filter unit with 100 kDa cutoff (Millipore, UFC910024). The resulting proteins were aliquoted and stored at −80 °C before use. The His-tagged SUMO protease was purified similarly, except washing buffers 1 and 2 contained 10 mM and 20 mM imidazole, respectively.

Cation exchange chromatography was performed for further purification of RBD#3L, RBD#4L, WT, and their HEPN2 domain mutants (R1046A/H1051A). After overnight dialysis, proteins were loaded onto a MonoS cation exchange column (Cytiva) via fast protein liquid chromatography (AKTA PURE, GE Healthcare) and eluted over a salt gradient from 300 mM to 1 M NaCl in buffer containing 20 mM Tris-HCl (pH 8.0) and 2 mM DTT. Fractions were collected and visualized by SDS-PAGE with Coomassie blue staining for the presence of desired proteins. Pooled fractions were buffer exchanged and concentrated to ~15 µM. Proteins were stored in buffer containing 20 mM Tris-HCl pH 7.5, 600 mM NaCl, 2 mM DTT, and 35% glycerol, aliquoted, flash-frozen in liquid nitrogen, and stored at −80 °C before use (Supplementary Fig. 11).

RNA target and crRNA preparation. Non-labeled RNA targets (T1–T29) and crRNAs (cr4–cr19; Supplementary Notes 2 and 3) were obtained by in vitro transcription (IVT) using the HiScribe T7 Quick High Yield RNA Synthesis Kit (NEB, E2050S). IVT templates for T1–T3 and T27–T29 were PCR amplified from gBlock (IDT) containing a T7 promoter sequence, and templates for crRNAs were PCR amplified using a universal forward primer (Pr01) and a reverse primer (Pr02–Pr17; Supplementary Note 5). PCR products were gel purified and eluted with nuclease-free water. The concentration and purity of the templates were measured by Nanodrop. At least 1 pmol of DNA was added to each IVT reaction.

IVT templates for T4–T26 were obtained by annealing the top primer Pr18 with the bottom primer Pr38, annealing top primer Pr22 with bottom primer Pr23–Pr37 or Pr39–Pr44, or annealing the top primer Pr45 with bottom primer Pr46 (Supplementary Note 5). In brief, a final concentration of 10 µM top and bottom primers were added to a 10-µl reaction containing 1 µl 10× Standard Taq buffer (NEB, B9014S). Annealing was performed in a thermocycler by heating the oligonucleotides to 95 °C and cooling them down to room temperature at 1 °C min^{-1}. The 10-µl annealing reactions were directly used as IVT templates.

A 40-µl IVT reaction was performed by mixing DNA template with 2.5 mM nucleoside triphosphates, 2 µl T7 polymerase, and 1 U µl^{-1} Murine RNase Inhibitor (NEB, M0314L), followed by incubation at 37 °C for 4 h. The IVT products were treated with DNase I and purified with either RNAClean XP beads (Beckman Coulter, A63987)[9] (for T4–T25), or by urea-PAGE gel electrophoresis followed by acid phenol–chloroform extraction. In brief, bands were excised, crushed, and suspended in five volumes of 0.3 M NaOAc (pH 5.2, Thermo Scientific, R1181), and subjected to four repeated cycles of 15-min freezing at −80 °C and quick thawing at room temperature. The elute was filtered and mixed with an equal volume of phenol:chloroform:iso-amyl alcohol (125:24:1, pH 4.5; Sigma-Aldrich, P1944), then centrifuged at 13,000*g* and 4 °C for 10 min. The upper aqueous phase was re-extracted by an equal volume of chloroform:iso-amyl alcohol (24:1; Sigma-Aldrich, C0549) twice. For every 400 µl of washed upper phase, 1 µl RNA-grade glycogen (Thermo Scientific, R0551) was added as an inert carrier of RNAs, then mixed thoroughly with 400 µl of isopropanol to precipitate at −20 °C for 1 h. The resulting RNA pellet was washed with 70% ice-cold ethanol twice, air-dried, and redissolved in nuclease-free H_2O. The RNA concentration and purity were measured with Nanodrop and the identity was confirmed by denaturing gel electrophoresis.

The body-radiolabeled target RNAs were in vitro transcribed in each 20-µl reaction containing 50 ng µl^{-1} DNA template, 2 mM each nucleoside triphosphate, and 5 U µl^{-1} T7 polymerases in reaction buffer (100 mM HEPES-KOH, pH 7.5, 30 mM DTT, and 2 mM spermidine supplemented with 0.34 µM α-[^{32}P]-ATP (3,000 Ci mmol^{-1}; PerkinElmer, BLU003H250UC)), with 20 mM or 8 mM $MgCl_2$ for target RNA T1 or T26, respectively. Reactions were incubated at 37 °C for 3 h and subsequently purified with Illustra MicroSpin G-50 columns (GE Healthcare, 27-5330-02), and eluted with 20 µl TE buffer (20 mM Tris-HCl, pH 8.0, and 1 mM EDTA). The concentration of body-radiolabeled target RNAs was measured with Nanodrop. The eluted RNA was aliquoted and stored at −20 °C if not immediately used.

Targets, crRNAs, and IVT primers are listed in Supplementary Notes 2, 3 and 5.

Simulation sample preparation. The VTM (BioVision, M1515-50, Lot 7F14M15150), pooled human saliva (Innovative Research, IRHUSL5ML-34462), and pooled human urine (Innovative Research, IRHUURE50ML-35650) were supplemented with 1 M TCEP, 500 mM EDTA, and RNase inhibitor (40 U µl^{-1}) at a volume ratio of 100:11.39:0.23:2.28 with final concentrations of 87% biofluids, 100 mM TCEP, 1 mM EDTA, and 0.8 U µl^{-1} inhibitors. The pooled human serum (Innovative Research, ISER10ML-34238) and pooled human plasma (Innovative Research, IPLANAC10ML-33897) were diluted with PBS and supplemented with 1 M TCEP, 500 mM EDTA, and RNase inhibitor (40 U µl^{-1}) at a volume ratio of 100:251.2:40:0.8:8 with final concentrations of 25% serum or plasma, 100 mM TCEP, 1 mM EDTA, and 0.8 U µl^{-1} inhibitors. Synthetic targets were spiked into the biofluids and treated with the HUDSON method[28,36–38] (Supplementary Table 6). The heating steps were performed on a thermocycler (BioRad).

SARS-CoV-2 heat-inactivated and clinical sample treatment. Heat-inactivated SARS-CoV-2 samples from infected Vero E6 cell lysate and culture supernatant were purchased from ATCC (VR-1986HK) with a viral load of 3.9×10^5 copies per microliter (Lot #70042082).

Clinical samples were leftover specimens of nasopharyngeal swabs in VTM from SARS-CoV-2 infected patients or suspects from the Department of Pathology Microbiology laboratory at UConn Health. Nasopharyngeal swabs in VTM were obtained from hospitalized patients at UConn Health or outpatients at the UConn drive through COVID testing center. After isolation of the viral target, clinical samples were amplified by Transcription Mediated Amplification (TMA) or RT–qPCR to detect either the ORF1ab (including pp1ab), E1 (viral envelope), and/or N2 (nucleocapsid 2) target sequences. Ethical approval of the study was provided by the UConn Health Institutional Review Board. Positive or negative samples as

VTM leftovers were inactivated at 60 °C for 30 min before transfer to Zhang Lab at the Institute of Materials Science at UConn.

The heat-inactive cultivated or clinical virus samples were mixed with Quick Extract DNA Extraction Solution (Lucigen, QE09050) with a 1:1 volume ratio and incubated at 95°C for 5 min in a water bath to actively lyze viral particles and inactivate nucleases in samples[35,40]. The purchased viral samples were serially diluted in nuclease-free water at various concentrations before use. The treated clinical samples were directly used for detection.

Fluorescence plate reader assay. Fluorescence assays were performed as described[3] with modifications. The protein stock was diluted to 450 nM using the storage buffer (50 mM Tris-HCl, 600 mM NaCl, 5% glycerol, and 2 mM DTT, pH 7.5). The crRNA was diluted to 450 nM using nuclease-free water. Then, the ribonucleoprotein (RNP) was formed by mixing protein and crRNA in a ratio of 2:1 (v:v) at room temperature for 30 min. The 10-µl reactions contained 45 nM WT or RBD–LwaCas13a fusion protein, 22.5 nM crRNA, 125 nM reporter, 1 U µl^{-1} RNase Inhibitor, 10–50 pM targets, and the reaction buffer (50 mM Tris-HCl, 5 mM Mg^{2+}, pH 8.0), unless otherwise indicated.

For Figs 1b,c, 2d,g, 3c,d and 4, Extended Data Figs 1b,c, 2 and 4, and Supplementary Figs 1–3, the reactions were initiated by adding eight parts of the master mix containing RNP, RNase Inhibitor, Tris, and Mg^{2+} (or buffer as indicated) to two parts of the mixture containing an equal volume of target and reporter. The controls were performed in parallel using the same amount of nuclease-free water to replace the targets.

For Fig. 5 and Extended Data Figs 7 and 8, the reactions were initiated by adding eight parts of the master mix containing RNP, RNase Inhibitor, reporter, Tris, and Mg^{2+} to two parts of the mixture containing the targets, background RNA, and biofluid/water. The controls were performed in parallel using the same amount of nuclease-free water instead of the targets in the presence or absence of the biofluid.

All reactions were performed in a 384-well microplate (Greiner, 784900) at 37 °C, with fluorescence monitored every 2 min over 30–120 min on a TECAN infinity M200 plate reader (excitation: 490 nm, emission: 520 nm, gain: 100; or excitation: 485 nm, emission: 528 nM, gain: 150 for reactions in Extended Data Fig. 4, Supplementary Figs 2 and 3).

Targets, crRNAs, and reporters used in each reaction are listed in Supplementary Notes 2–4.

Fluorescence gel assay. Reactions were carried out as described above in the fluorescence plate reader assay, except the fluorophore–quencher reporters were replaced by 5′-FAM-labeled U_5, U_{11}, U_{15}, or U_{20} (r2, and r4–6; Supplementary Note 4). Reactions with a total volume of 110 µl was initiated by adding target RNA (T1) at a final concentration of 10 pM. Aliquots of 20-µl reaction were removed at 0, 5, 10, 15, and 30 min, quenched by mixing with an equal amount of 2× loading buffer (93.5% formamide, 0.025% xylene cyanol FF, and 20 mM EDTA, pH 8.0), incubated at 95 °C for 5 min, and snap cooled on ice. Quenched reactions were resolved on 22.5% (v/v) denaturing polyacrylamide gel, then visualized and captured with a Sapphire Biomolecular Imager (Azure Biosystems). Assays were performed in three technical replicates, and the band intensity of the substrates and products was analyzed using ImageJ. The percent cleavage of each reporter was determined as the ratio of band intensity of all cleavage products to the total intensity within the lane, that is, the sum of intensity from the cleaved and uncleaved reporter, and normalized for the background of each measured reporter.

Electrophoretic mobility shift assay. To quantify the target binding affinity, assays were carried out in binding buffer (50 mM Tris-HCl, pH 8.0, 60 mM NaCl, 5 mM $MgCl_2$, 1 mM DTT and 10% glycerol) with a serial dilution of the protein:crRNA complex (protein:crRNA = 1:0.95, protein from 5 nM to 288 nM). HEPN2 mutants dRBD#3L, dRBD#4L, and dWT LwaCas13a, were respectively complexed with crRNA (cr1; Supplementary Note 3) for 30 min at room temperature, then incubated with 5 nM body-radiolabeled RNA targets (T1 or T26; Supplementary Note 2) for another 30 min at room temperature, and further incubated at 37 °C for 10 min. Each sample was mixed with a loading buffer containing 10% glycerol and 0.05% bromophenol blue before loading onto a 5% native polyacrylamide gel containing 0.5× TBE buffer. The gel was pre-run at 4 °C for 45 min at 120 V with 0.5× TBE as a running buffer. Gels were dried on filter paper with a HydroTech Pump Gel Drying Complete System (BioRad), followed by exposure to a phosphorimager plate for 48 h, and imaged using phosphorimaging by the Sapphire Biomolecular Imager (Azure Biosystems).

The reporter binding affinity assay was carried out in binding buffer (50 mM Tris-HCl pH 7.5, 60 mM NaCl, 5 mM $MgCl_2$, 1 mM DTT, 5% glycerol, and 0.01% Triton X-100). The RNP complex was formed by incubating the protein and crRNA at room temperature for 30 min and serially diluted with the binding buffer (protein:crRNA = 2:1, protein from 50 nM to 2 µM). To mimic the target-activated protein complex and avoid competitive target binding, an equal amount of 50 pM of the target RNA was added to each of the RNP dilutions and incubated at 37 °C for 30 min. The reactions were further incubated with 100 nM of 5′-FAM-labeled U_{20} reporter (r6; Supplementary Note 4) for 10 min at 37 °C. Each sample was mixed with a loading buffer containing 10% glycerol and 0.05% bromophenol blue before loading onto a 6% native polyacrylamide gel containing 1× TG buffer at 4 °C (25 mM Tris base, 250 mM glycine). The gels were pre-run at 4 °C for 45 min at 120 V with 1× TG running buffer and visualized with a Sapphire Biomolecular Imager (Azure Biosystems). All experiments were carried out with two technical replicates. The bound and unbound fraction of target or reporter RNA was quantified by using Azure Spot (Azure Biosystem), plotted in GraphPad Prism, and fitted by non-linear regression with saturation one-site binding.

Michaelis–Menton kinetic study. For Michaelis–Menten analysis, reactions were prepared by incubating 45 nM protein (WT/RBD#3L/RBD#4L) with 22.5 nM crRNA (cr1) to form the RNP in reaction buffer at room temperature for 30 min, followed by incubating at 37 °C for 10 min with 50 pM RNA targets (T1). Collateral cleavage was initiated by adding two parts of the substrate (r3; Supplementary Note 4) at various concentrations, that is, 6400, 3200, 1600, 800, 400, 200, 100, and 50 nM, to eight parts of the target-activated RNP and incubated at 37 °C on an M200 plate reader with fluorescence taken every 30 s for up to 10 min (excitation: 490 nm, emission: 520 nm). Reactions (10 µl) were performed on a 384-well microplate, with four technical replicates from two independent experiments in buffer containing 50 mM Tris, pH 8.0, 5 mM $MgCl_2$, and 1 U µl^{-1} RNase Inhibitor (Extended Data Fig. 6); or with four technical replicates in buffer containing 50 mM Tris, pH 8.0, 5 mM $MgCl_2$, 1 U µl^{-1} RNase Inhibitor, 100 µg ml^{-1} BSA, and 0.01% Triton X-100 (Supplementary Fig. 5).

To convert the time-course fluorescence signal ($F_{[U11]}$) to the molarity of cleavage products ([Cleaved U_{11}]), the reporters were serially diluted using the reaction buffers mentioned above, in the presence or absence of 50 µg ml^{-1} RNaseA (NEB, T3018L), to the same concentrations as in the assay. The level of fluorescence from quenched reporters (no RNaseA, $F_{0,[U11]}$) and completely cleaved reporters (RNaseA treated, $F_{F,[U11]}$) at each concentration was recorded for up to 30 min at 37 °C until reaching equilibrium. The molarity of cleavage products at each time point was calculated using the following equation (1):

$$[\text{Cleaved } U_{11}] = \frac{F_{[U_{11}]} - F_{0,[U_{11}]}}{F_{F,[U_{11}]} - F_{0,[U_{11}]}} \times [U_{11}] \quad (1)$$

where $[U_{11}]$ = 6400, 3200, 1600, 800, 400, 200, 100, and 50 nM.

Since the cleavage of 1 nM reporter produced similar levels of fluorescence signal with an average ~25–28 AU nM^{-1} at all tested reporter concentrations, the above equation (1) was then simplified to equation (2):

$$[\text{Cleaved } U_{11}] = \frac{F_{[U_{11}]} - F_{0,[U_{11}]}}{\text{Average}\left(\frac{F_{F,[U_{11}]} - F_{0,[U_{11}]}}{[U_{11}]}\right)} \quad (2)$$

The cleaved product molarity versus time was fitted by linear regression (GraphPad). The slope as initial velocity (nM s^{-1}) was plotted as a function of substrate concentration $[U_{11}]$ (nM), and further fitted to the Michaelis–Menten model (GraphPad) to determine kinetic parameters k_{cat}, and K_M. The enzyme concentration was constrained to 0.05 nM as the concentration of the target served as the proxy for that of activated enzymes.

Gold screen-printed electrode functionalization. The gold (Au)-SPE (C223BT, Metrohm) was first sonicated in acetone for 5 min to remove the impurity on the surface, followed by rinsing with deionized water for 30 s, drying by ultra-high pure nitrogen gas, and electrochemical cleaning by cycling voltammetry (CV) between −0.3 to 1.0 V in 0.1 M phosphate buffer (0.038 M NaH_2PO_4 and 0.061 M Na_2HPO_4, pH 7.4) versus a built-in Ag pseudo-reference electrode. The cleaned SPE was then rinsed with deionized water and dried by blowing ultra-high pure nitrogen gas. Thiol-linked U_{20} reporter with methylene blue (r7; Supplementary Note 4) was reduced with 10 mM TCEP-HCl for 10 min to break the disulfide bond before use. A total of 25 µL of 2.5 µM reduced U_{20} reporter was cast on the 1.6-mm-diameter WE with 2-h incubation at room temperature to form a close-packed self-assembled monolayer through the thiol–gold interaction. The SPE was then rinsed with 10 mM Tris buffer (pH 8.0) and subsequently incubated in 2 mM 6-mercapto-1-hexanol (Sigma-Aldrich, 451088) for 30 min. The alkanethiol layer serves as an insulator to reduce the background current while spacing U_{20} molecules. Finally, the SPE was rinsed with 10 mM Tris buffer for 30 s to remove the physically adsorbed U_{20}. A final amount of approximately 50 pmol of reporters was attached to the surface of the WE (Supplementary Fig. 8). The functionalized SPE was stored in 10 mM Tris buffer at 4°C before use.

Endpoint Cas13a–electrochemical measurement. We first prepared the CRISPR–Cas master mix by adding the following components in a tube with a top-down order, and two CRISPR reaction conditions were used (Supplementary Table 7). The prepared CRISPR assay was incubated in the dark at room temperature for 10 min before adding to the WE for collateral cleavage.

Electrochemical measurements were performed using an Autolab N Series Potentiostat. To measure the voltammetric responses, a volume of 40 µl of 10 mM Tris buffer (pH 8.0) containing 100 mM NaCl was dropped on the SPE to serve as the electrolyte. SWV (with a frequency of 20 Hz and 50 mV amplitude superimposed on a DC ramp from −0.5 V to 0 V versus the Ag reference electrode)

was recorded from the U_{20} reporter functionalized WE. The initial current was recorded before adding the CRISPR assay. Then the sensor was rinsed with nuclease-free water to remove the electrolyte and dried with nitrogen. The 20-µl reaction was added onto the WE and incubated at room temperature for 30 min, terminated by Proteinase K (25 µg ml^{-1} final; Thermo Scientific, EO0491) treatment. The sensor was rinsed, dried, and added with the electrolyte for SWV measurement of the final current. The SWV peak current before (ipc_{before}) and after (ipc_{after}) the reaction was obtained from the built-in peak search function of the potentiostat software NOVA2.1. ΔI% was calculated from the SWV peak current by equation (3)

$$\Delta I\% = \frac{(ipc_{before} - ipc_{after})}{ipc_{before}} \times 100\% \quad (3)$$

The theoretical LoD was determined by equation (4)

$$LoD = 3 \times SD_{blank}/m \quad (4)$$

where m is the slope of the best fitting line (sensor response to different target concentrations), and SD_{blank} is the standard deviation of blank experiments (non-target control).

Time-course Cas13a–electrochemical measurement. Time-course voltammetric responses of Cas13 assays were obtained by SWV every 30 s over 2 min to measure the initial velocity of reaction, and over 20 min to record the full course. Each SWV measuring cycle included 5 s of deposition at a potential of −0.38 V to entirely reduce the MB for a maximal electron transfer, 5 s of the SWV measurement to obtain the peak current, followed by 20 s of waiting time. Before the reaction, 35 µl electrolyte was dropped on the WE and the initial peak current (ip_0) was obtained after 5–10 cycles of SWV scan for signal stabilization. A volume of 5 µl pre-assembled Cas13 reaction was then gently dispersed into the electrolyte with final concentrations of each component of reaction the same as described in Supplementary Table 7 (Tris-buffered) with extra Tris (8.75 mM) and NaCl (87.5 mM) from the electrolyte. The peak current from each time point (ip_t) was normalized to the corresponding initial peak current (ip_0) and plotted as a function of the time. To eliminate the background signal for curve fitting, the fold change of the normalized peak current of the target-containing reactions to that of the non-target controls (equation (5)) was calculated for each time point and then fitted with one-phase decay to determine the pseudo-first-order rate constant k_{obs} (GraphPad).

$$(\text{Background corrected peak current})_t = \frac{(ip_t/ip_0)_{target}}{(ip_t/ip_0)_{NTC}} \quad (5)$$

where t is the SWV scan time (0, 30, 60, 90 s etc.).

Clinical sample RNA extraction and RT–qPCR. RNA for RT–qPCR detection was purified from 140 µl VTM leftover for the storage of clinical nasopharyngeal swab and eluted to 80 µl elution buffer using the QIAamp Viral RNA Mini Kit (Qiagen, 52904) per manufacturer's protocols. Purified RNAs were aliquoted and stored at −80 °C. RT–qPCR quantification was performed according to Centers for Disease Control and Prevention instructions using 2019-nCoV RUO Kit (IDT, 10006713; N1-Forward: 5′-GACCCCAAAATCAGCGAAAT-3′; N1-Reverse: 5′-TCTGGTTACTGCCAGTTGAATCTG-3′; N1-Probe: FAM-ACCCCGCATTACGT TTGGTGGACC-BHQ1) and GoTaq Probe 1-Step RT–qPCR System (Promega, A6120) on a CFX96 Touch Real-Time PCR Detection System (BioRad) with the following cycling conditions: hold at 25 °C for 2 min, reverse transcription at 45 °C for 15 min, hold at 95 °C for 2 min, followed by 45 cycles with DNA denaturation at 95 °C for 3 s, and annealing and elongation at 55 °C for 30 s. Data were analyzed using CFX Maestro Software.

Reporting summary. Further information on research design is available in the Nature Research Reporting Summary linked to this article.

Data availability

All data generated or analyzed during this study are included in this published article and its Supplementary Information. The previous structural data that support the findings of this study are available in the PDB (IDs: 5XWP, 5MPL, and 2MXY). Source data are provided with this paper.

Acknowledgements

We thank P. Lillehoj for proofreading the manuscript. We acknowledge funding from NSF CBET-2031242, Welch Foundation (C-1952), and Rice University Startup fund (to X.G.); the University of Connecticut Startup fund and NSF CBET-2103025 (to Y.Z.); and the Welch Foundation (C-2033-20200401) and the Cancer Prevention & Research Institute of Texas (CPRIT) Award RR190046 (to Y.G.).

Author contributions

X.G. designed and supervised the research. J.Y., Y.G., and X.G. conceived and designed the RBD fusion protein engineering. Y.G. performed the structural analysis. J.Y. and X.D. expressed and purified proteins, and transcribed and purified RNAs. J.Y. performed the experiments and analyzed the data related to nuclease activity fluorescence plate reader assay, kinetic analysis, and gel assay, with the assistance of J.A.V. and Z.Y. X.D. performed gel shift assays and analyzed the data. Yi.Z. and Y.S. conceived and designed the Cas13a–electrochemical system. Y.S. and Z.W. performed the experiments related to the Cas13a–electrochemical system, and J.Y., Y.S., and Z.W. analyzed the data. L.A. and K.D.D. provided and verified the clinical samples. Y.S. and Yu.Z. performed RT–qPCR and analyzed the data. J.Y. performed and analyzed results from all other experiments with assistance from J.A.V., Z.Y. and A.P. J.Y., Y.S., and X.G. drafted the manuscript with input from all authors.

Competing interests

X.G., J.Y., and Y.G. are co-inventors on a provisional patent application 63/285,304 (filed) relating to the engineered Cas13 variants described in this manuscript. The remaining authors declare no competing interests.

Additional information

Extended data is available for this paper at https://doi.org/10.1038/s41589-022-01135-y.

Supplementary information The online version contains supplementary material available at https://doi.org/10.1038/s41589-022-01135-y.

Correspondence and requests for materials should be addressed to Yang Gao, Yi Zhang or Xue Gao.

Peer review information *Nature Chemical Biology* thanks the anonymous reviewers for their contribution to the peer review of this work.

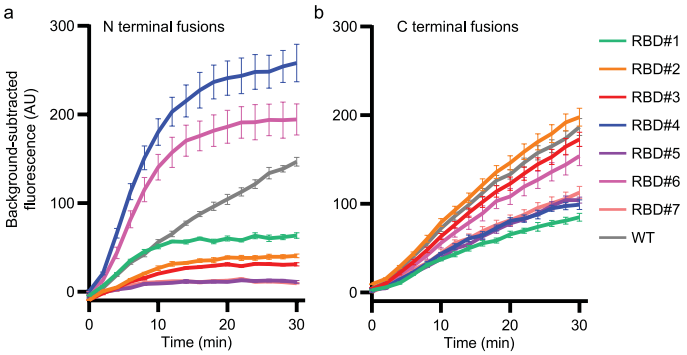

Extended Data Fig. 1 | Time course of N- and C- terminal RBD fusions. a and b, Background-subtracted fluorescence in the detection of 10 pM synthetic SARS-CoV-2 N gene fragment targets (T1) using N- (**a**) and C- (**b**) terminal RBD fusions, expressed as mean ± s.e.m. from four technical replicates.

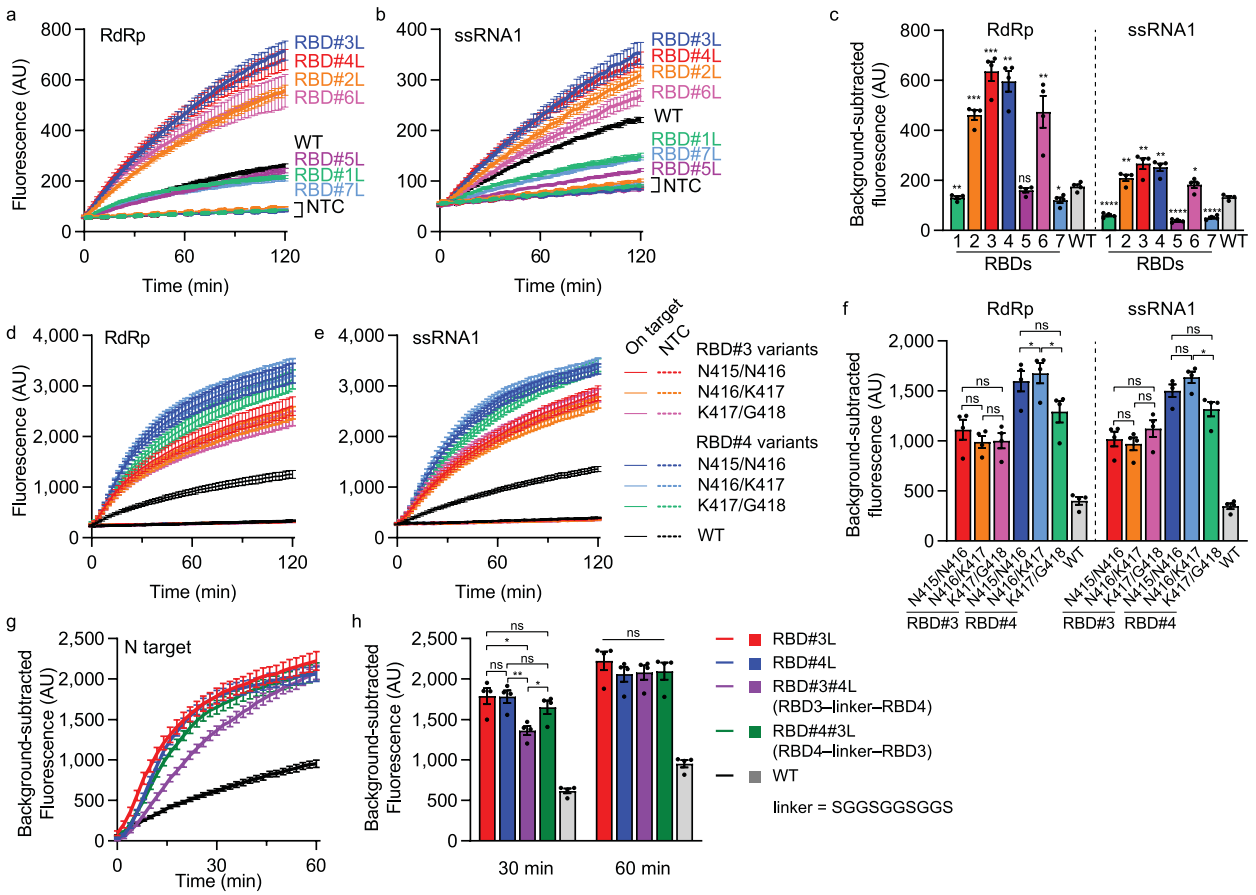

Extended Data Fig. 2 | Testing of RBD loop-fusion variants. Each of the fusion proteins was assembled with the crRNA as described in Methods. **a–c**, Testing of seven candidate RBDs (RBD#1–RBD#7) fused to LwaCas13a. **a and b**, Raw fluorescence over a course of 120 min in the reactions with or without 10 pM synthetic RNA targets: **a**, SARS-CoV-2 RdRp gene fragment (T2); **b**, ssRNA1 (T3). NTC, non-target control. **c**, The 120-min background-subtracted fluorescence from **a and b**. **d–f**, Testing of RBD#3 and RBD#4 fused to various positions on Loop 1 of LwaCas13a. The six variants were RBD#3 and #4 inserted after N415, N416, and K417, respectively. **d and e**, Raw fluorescence data over a course of 120 min in the reactions with or without 10 pM synthetic RNA targets: **d**, SARS-CoV-2 RdRp gene fragment (T2); **e**, ssRNA1 (T3). **f**, The 30-min background-subtracted fluorescence from **d and e**. **g and h**, Testing of tandem RBD insertions. The four variants for comparison were RBD#3, RBD#4, RBD#3–linker–RBD#4, and RBD#4–linker–RBD#3 inserted after N415 on Loop 1 of LwaCas13a, respectively. A 10-aa flexible linker (SGGSGGSGGS) was used to connect two RBDs in tandem. **g**, Background-subtracted fluorescence data over a course of 60 min in the reactions with 10 pM SARS-CoV-2 N gene fragment synthetic RNA targets (T1). **h**, The 30-min and 60-min background-subtracted fluorescence from **g. a, b, d, e, and g**, Lines and error bars represented mean ± s.e.m. from four technical replicates; **c, f, and h**, bar plots were expressed as mean ± s.e.m. from four technical replicates. Two-tailed *p* values were calculated using unpaired t-tests with Welch's correction: ns, not significant, $^{*}p < 0.05$, $^{**}p < 0.01$, $^{***}p < 0.001$, $^{****}p < 0.0001$ (see SourceData for *p* value).

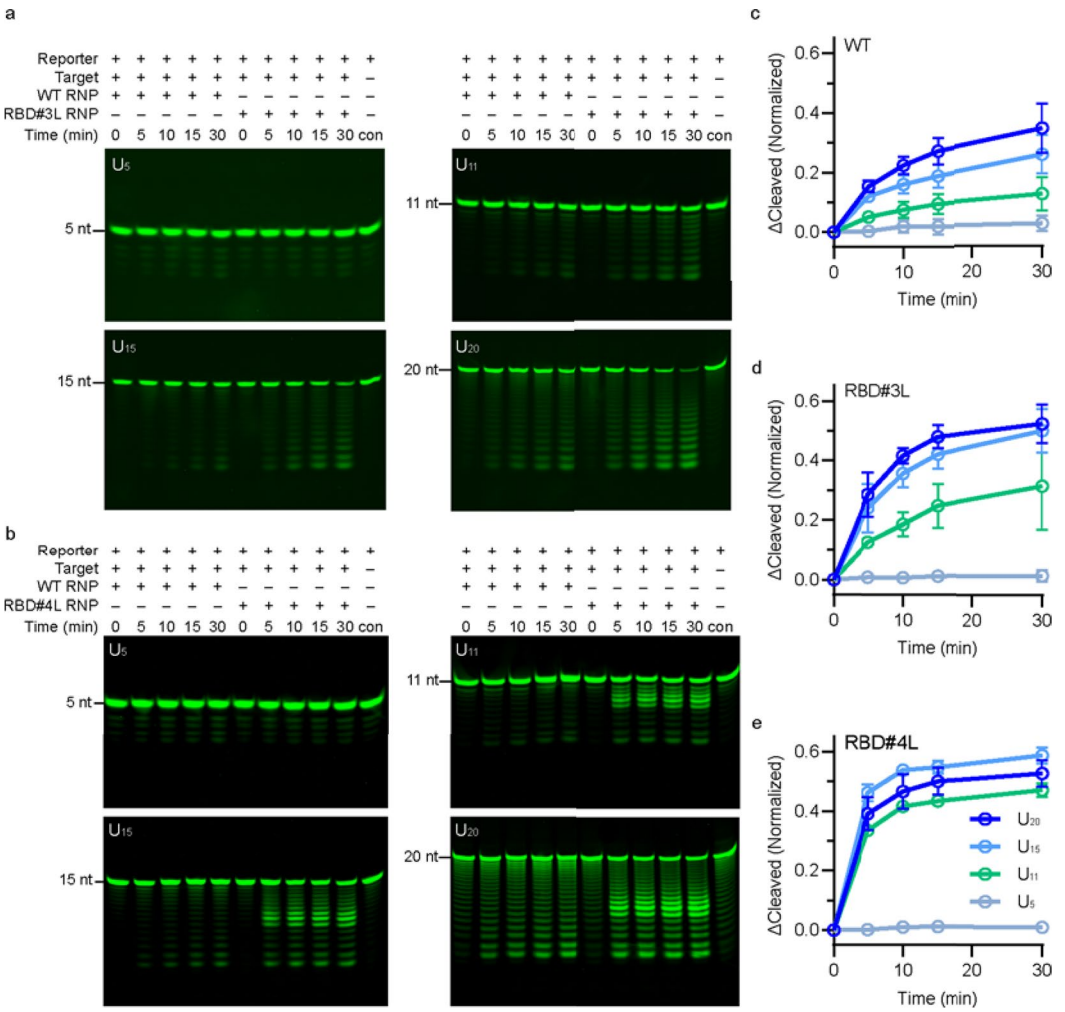

Extended Data Fig. 3 | Optimizing reporter length for enhanced collateral activity. a and b, Representative gel images of the cleavage of 5′-FAM-labeled U_5, U_{11}, U_{15}, and U_{20} reporters by WT LwaCas13a, RBD #3L, and RBD#4L over 0–30 min. RBD fusions and WT were tested side-by-side. **c–e**, Quantified percentage of cleaved products as shown in **a and b**, represented by mean ± s.e.m. of three technical replicates from two independent experiments. Gels were analyzed by ImageJ. The percentage of cleaved products was calculated by the intensity of product bands divided by the summed intensity of the product and substrate bands within one lane and normalized to the reporter-only control.

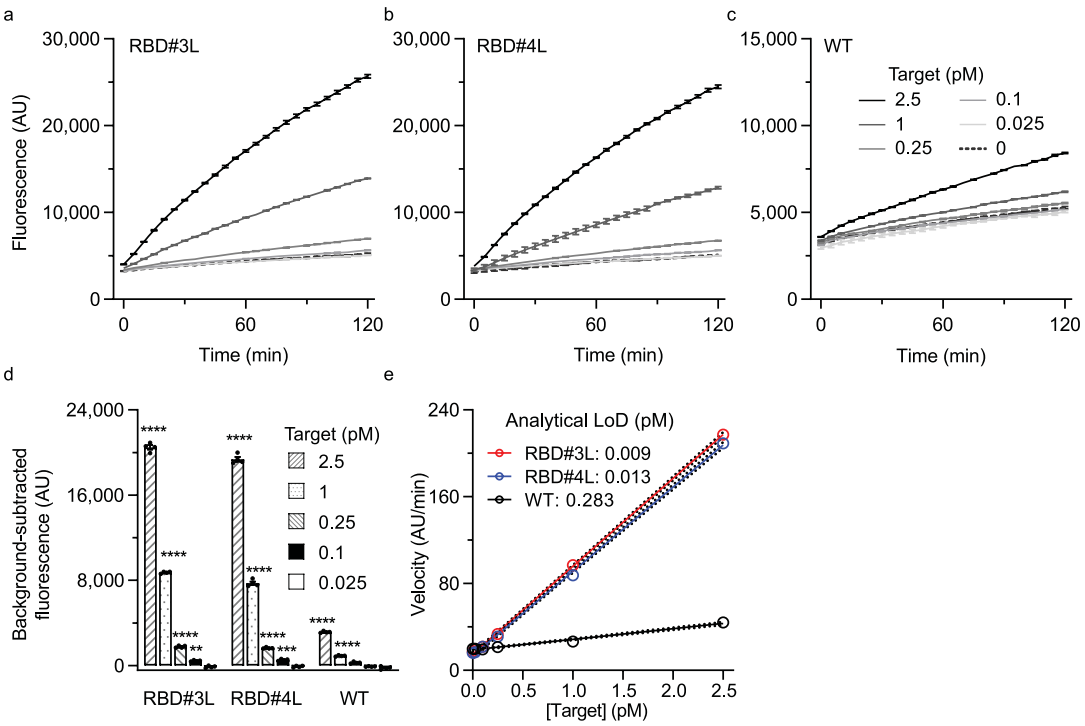

Extended Data Fig. 4 | LoD analysis of RBD#3L, RBD#4L, and WT LwaCas13a in reactions supplemented with BSA and Triton X-100. a–c, Raw fluorescence data measured for 120 min, expressed as mean ± s.e.m. from four technical replicates. RBD#3L, RBD#4L and WT LwaCas13a were complexed with crRNA (cr1) and tested with 2.5, 1, 0.25, 0.1, 0.025 pM of the synthetic RNA (T1) in reaction buffer supplemented with 100 μg/mL BSA and 0.01% Triton X-100 (as in Supplementary Fig. 2b). The 0 pM target samples were used as non-target control (NTC). **d**, The bar plot represented the 120-min background-subtracted fluorescence expressed as mean ± s.e.m. from four technical replicates. Adjusted *p* values were calculated using two-way ANOVA with Dunnett's test: $^{**}p = 0.0059$, $^{***}p = 0.0007$, $^{****}p < 0.0001$, compared to background signal (non-target control) (see SourceData for adjusted *p* value). **e**, The velocities of each reaction within 60 min were obtained by linear regression from **a–c** and were plotted as functions of the target concentration. Outliers were identified by the ROUT method with a Q = 5%. Analytical LoD of three proteins was listed in Supplementary Table 2.

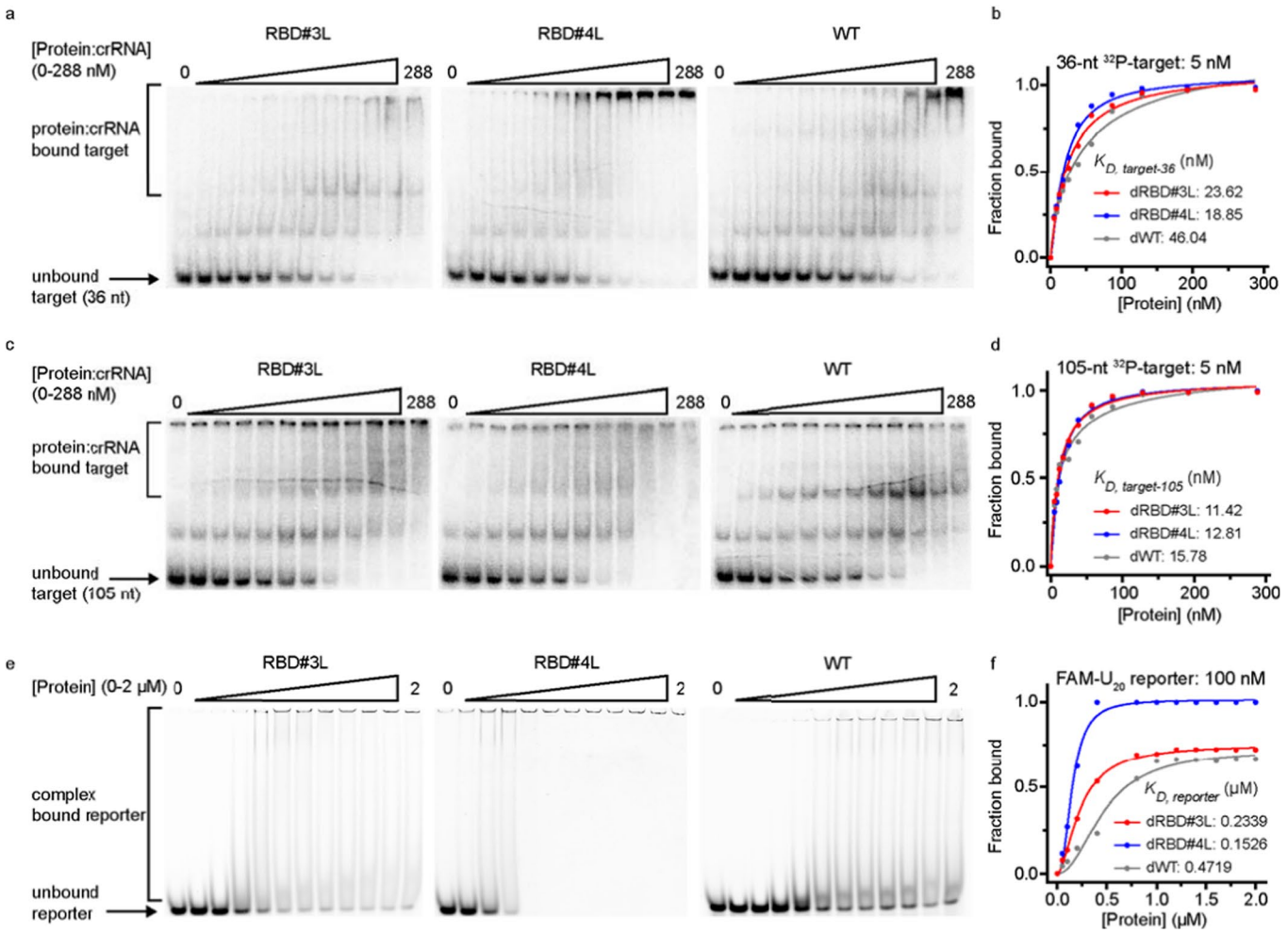

Extended Data Fig. 5 | Quantification of RNA binding with RBD#3L, RBD#4L, and WT LwaCas13a. a and c, Representative EMSA gel images of inactive HEPN2 mutants (R1046A/H1051A), that is, dRBD#3L, dRBD#4L, and dWT complexed with crRNA binding to 5 nM of body-radiolabeled (^{32}P) target RNA. (**a**, T26; **c**, T1). The protein:crRNA complex with a molar ratio of 1:0.95 was serially diluted to 288, 192, 128, 86, 57, 38, 25, 17, 12, 8 and 5 nM. The 0-nM control was target RNA with reaction buffer. **b and d**, Calculation of binding affinity between target RNA and RNP. Bound and unbound fractions from **a and c** were quantified by densitometry and fitted to standard binding isoforms. Mean from two technical replicates was plotted. **e**, Representative EMSA gel images of protein:crRNA:target ternary complex binding with 100 nM of 5'-FAM-labeled U_{20} reporter. The dRBD#3L, dRBD#4L and dWT complex with crRNA with a molar ratio of 2:1 was serially diluted to 2, 1.8, 1.6, 1.4, 1.2, 1, 0.8, 0.4, 0.2, 0.1 and 0.05 μM. An equal amount of 50 pM non-labeled target (T1) was added to the RNPs to mimic the target-bound ternary complex. The 0-μM control was the reporter with reaction buffer. **f**, Calculation of binding affinity between reporter RNA and target-bound RNP. Bound and unbound fractions from **e** were quantified by densitometry and fitted to standard binding isoforms. Mean from two technical replicates was plotted. Means of the dissociation constant with 95% CI are listed in Supplementary Table 3.

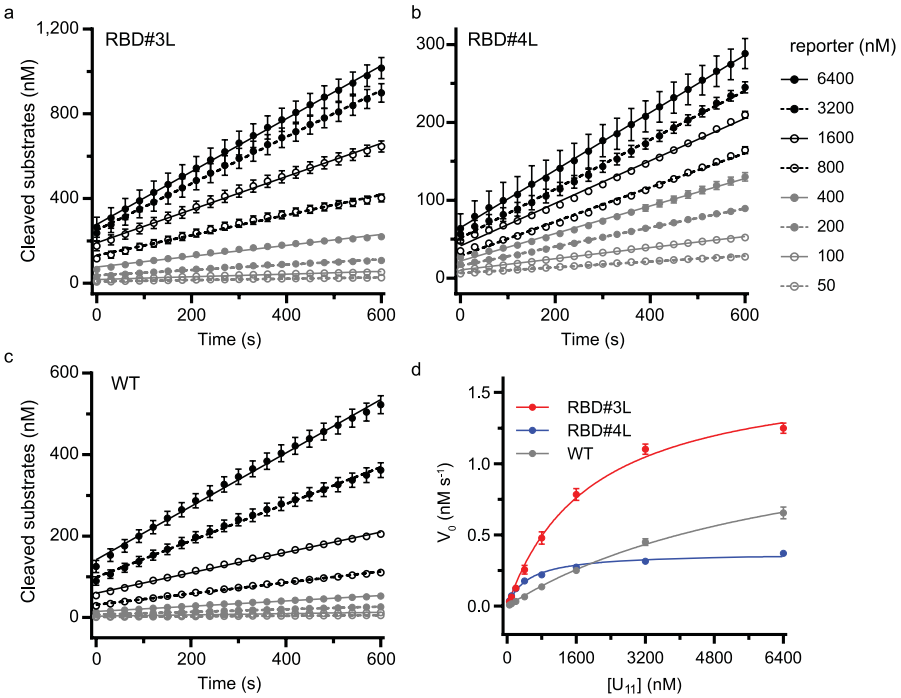

Extended Data Fig. 6 | Kinetic analysis of RBD#3L, RBD#4L and WT LwaCas13a. a–c, Progress curves of cleaved reporters versus time. Data were plotted as mean ± s.e.m. from two independent experiments each with four technical replicates. The RNP complex of RBD#3L, RBD#4L, and WT was incubated with 50 pM of the targets (T1) for 10 min at 37 °C prior to cleavage reaction using 6400, 3200, 1600, 800, 400, 200, 100 and 50 nM of the U_{11} substrates. The initial velocities (within 600 s) of each reaction were obtained by linear regression. **d**, Initial velocities from two independent experiments each with four technical replicates obtained from **a–c** were plotted as mean ± s.e.m. versus the U_{11} reporter concentration and fitted to a Michaelis-Menten curve. Summary of kinetic parameters are listed in Supplementary Table 4.

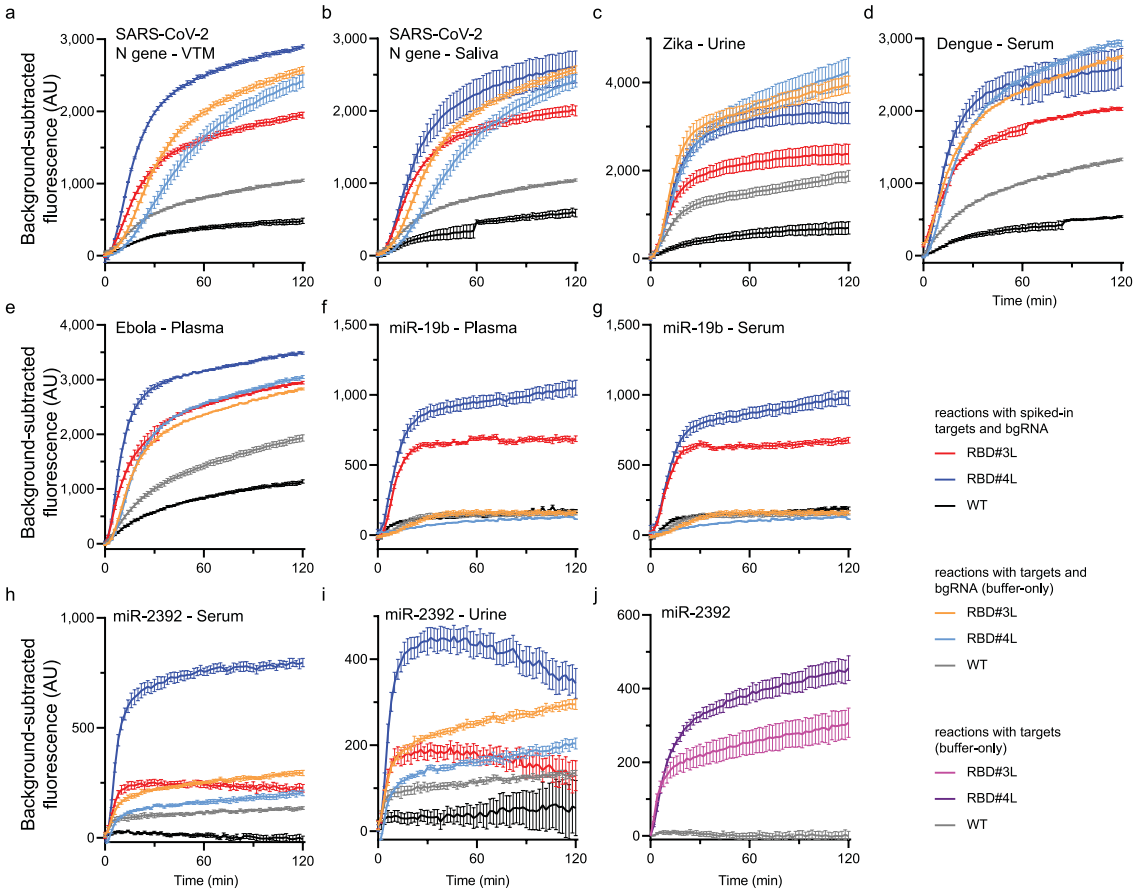

Extended Data Fig. 7 | Testing RBD#3L, #4L, and WT LwaCas13a in the detection of viral RNA and microRNA spiked-in samples. Background-subtracted fluorescence over 120 min in the detection of **a, b**, 10 pM of SARS-CoV-2 N gene synthetic targets spiked into 8% VTM, 8% saliva, or reaction buffer; **c**, 10 pM of Zika synthetic targets spiked into 8% urine, or reaction buffer, **d**, 10 pM of Dengue synthetic targets spiked into 2.5% serum, or reaction buffer; **e**, 10 pM of Ebola synthetic targets spiked into 2.5% plasma, or reaction buffer; **f, g**, 10 pM of miR-19b spiked into 2.5% plasma, 2.5% serum, or reaction buffer; **h, i**, 200 pM of miR-2392 spiked into 2.5% serum, 8% urine, or reaction buffer; **j**, 10 pM of miR-2392 in reaction buffer. All reactions were supplemented with 50 ng total RNA extracted from HEK293T cells but **j**. Background-subtracted fluorescence data were expressed as mean ± s.e.m. from four technical replicates (**a–i**), or 2 independent experiments, each with four technical replicates (**j**).

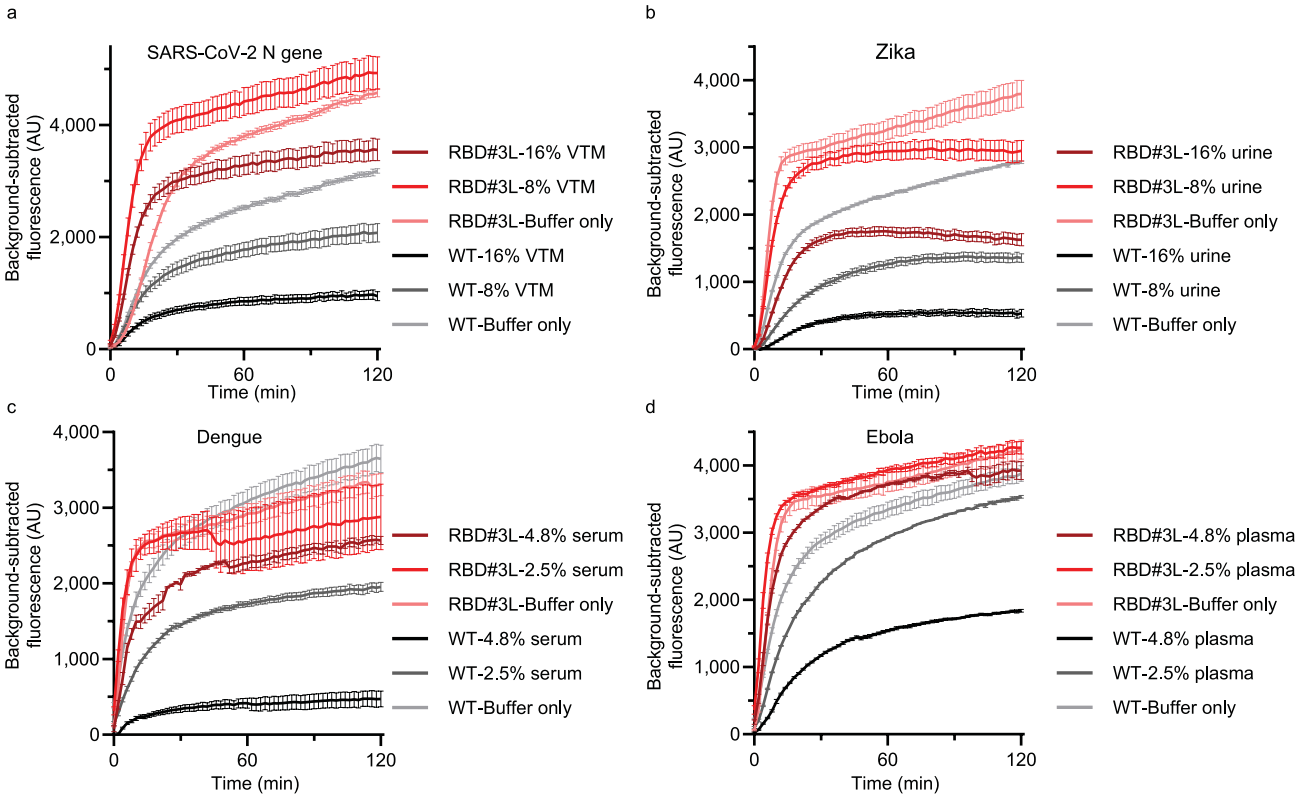

Extended Data Fig. 8 | Testing RBD#3L and WT LwaCas13a in the detection of viral RNA spiked-in samples. Background-subtracted fluorescence over 120 min in the detection of **a**, 50 pM SARS-CoV-2 N gene synthetic targets (T1) spiked into 16% VTM, 8% VTM, or reaction buffer; **b**, 50 pM of Zika synthetic targets (T27) spiked into 16% urine, 8% urine, or reaction buffer, **c**, 50 pM of Dengue synthetic targets (T28) spiked into 4.8% serum, 2.5% serum, or reaction buffer; **d**, 50 pM of Ebola synthetic targets (T29) spiked into 4.8% plasma, 2.5% plasma, or reaction buffer. All reactions were supplemented with 50 ng total RNA extracted from HEK293T cells as background. Background-subtracted fluorescence data were expressed as mean ± s.e.m. from four technical replicates.

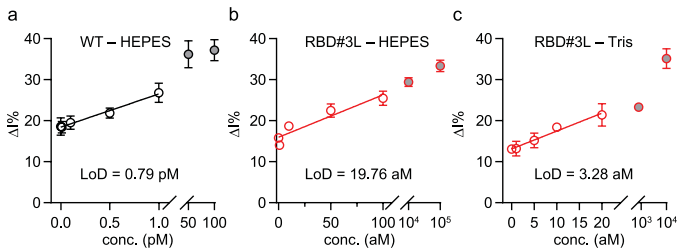

Extended Data Fig. 9 | Theoretical LoD of the WT LwaCas13a and RBD#3L coupled to the electrochemical sensor in the detection of synthetic RNA target. a, ΔI% (mean ± s.d. from three technical replicates) from Fig. 6a was plotted as a function of target concentration (0, 0.01, 0.1, 0.5, and 1 pM) and fitted by linear regression with replicate y values considered as individual data points. **b**, ΔI% (mean ± s.d. from three technical replicates) from Fig. 6b was plotted as a function of target concentration (0, 1, 10, 50, and 100 aM) and fitted by linear regression. **c**, ΔI% measurement from samples with activated RBD#3L RNP. The sample treatment and assay conditions were in parallel with Fig. 6b except the reaction buffer used was Tris (Supplementary Table 7). ΔI% (mean ± s.d. from three technical replicates) was plotted as a function of target concentration (0, 1, 5, 10, and 20 aM) and fit by linear regression. LoD values were 0.79 pM for WT, 19.76 aM for RBD#3L in HEPES buffer, and 3.28 aM for RBD#3L in Tris buffer, respectively.

nature portfolio

Corresponding author(s): Xue Gao

Last updated by author(s): Jun 15, 2021

Reporting Summary

Nature Portfolio wishes to improve the reproducibility of the work that we publish. This form provides structure for consistency and transparency in reporting. For further information on Nature Portfolio policies, see our Editorial Policies and the Editorial Policy Checklist.

Statistics

For all statistical analyses, confirm that the following items are present in the figure legend, table legend, main text, or Methods section.

n/a	Confirmed
☐	☒ The exact sample size (*n*) for each experimental group/condition, given as a discrete number and unit of measurement
☐	☒ A statement on whether measurements were taken from distinct samples or whether the same sample was measured repeatedly
☐	☒ The statistical test(s) used AND whether they are one- or two-sided *Only common tests should be described solely by name; describe more complex techniques in the Methods section.*
☒	☐ A description of all covariates tested
☐	☒ A description of any assumptions or corrections, such as tests of normality and adjustment for multiple comparisons
☐	☒ A full description of the statistical parameters including central tendency (e.g. means) or other basic estimates (e.g. regression coefficient) AND variation (e.g. standard deviation) or associated estimates of uncertainty (e.g. confidence intervals)
☐	☒ For null hypothesis testing, the test statistic (e.g. *F*, *t*, *r*) with confidence intervals, effect sizes, degrees of freedom and *P* value noted *Give P values as exact values whenever suitable.*
☒	☐ For Bayesian analysis, information on the choice of priors and Markov chain Monte Carlo settings
☒	☐ For hierarchical and complex designs, identification of the appropriate level for tests and full reporting of outcomes
☒	☐ Estimates of effect sizes (e.g. Cohen's *d*, Pearson's *r*), indicating how they were calculated

Our web collection on statistics for biologists contains articles on many of the points above.

Software and code

Policy information about availability of computer code

Data collection	Magellan V7.1; Nova 2.1; CFX Maestro 1.1.
Data analysis	Magellan V7.1; Nova 2.1; GraphPad Prism 8; OriginPro 2021b; Pymol2.5.2; RoseTTAFold; AlphaFold; Benchling; ImageJ 1.53e; Image Lab 6.1; Sapphire1.3

For manuscripts utilizing custom algorithms or software that are central to the research but not yet described in published literature, software must be made available to editors and reviewers. We strongly encourage code deposition in a community repository (e.g. GitHub). See the Nature Portfolio guidelines for submitting code & software for further information.

Data

Policy information about availability of data

All manuscripts must include a data availability statement. This statement should provide the following information, where applicable:

- Accession codes, unique identifiers, or web links for publicly available datasets
- A description of any restrictions on data availability
- For clinical datasets or third party data, please ensure that the statement adheres to our policy

All data generated or analysed during this study are included in this published article (and its supplementary information files). The previous structural data that support the findings of this study are available in PDB (ID: 5XWP, 5MPL and 2MXY).

Field-specific reporting

Please select the one below that is the best fit for your research. If you are not sure, read the appropriate sections before making your selection.

☒ Life sciences ☐ Behavioural & social sciences ☐ Ecological, evolutionary & environmental sciences

For a reference copy of the document with all sections, see nature.com/documents/nr-reporting-summary-flat.pdf

Life sciences study design

All studies must disclose on these points even when the disclosure is negative.

Sample size	No sample size calculation was performed. In case where statistics was derived, three or more replicates were used in each experiments. Clinical sample size was limited by the availability of leftover specimens in viral transportation media.
Data exclusions	For the buffer optimization experiments, one of the replicates was removed due to the pipetting error that the reaction mixture was not enough for the last replicate wells. For the clinical samples, two sets of data were excluded and experiments were repeated because of the systematic error (the reaction solutions were not well mixed).
Replication	All attempts at replication were successful. All fluorescence plate reader experiments were performed with four replicates. Fluorescence gel experiments, endpoint electrochemical experiments were performed in at least triplicates. Time course electrochemical experiments were performed with four replicates for the WT and RBD#3L and duplicates for RBD#4L due to the limited availability of the methylene blue labeled reporters.
Randomization	No randomization was performed. Samples and controls were assembled with the same reagents at the same concentrations and were tested side-by-side in a plate reader or an electrochemical sensor.
Blinding	The engineered Cas13 protein and wild-type Cas13 protein were shipped from Rice University Gao Lab with number (#1 and #2) and concentrations labeled. 1 pM synthetic RNA target was used to test both proteins. It turns out that the current change percentage for protein #1 was 34%, and 26.8% for #2. Protein #1 showed higher activity than #2. The result was consistent with the record from Gao Lab. Protein #1 was the engineered protein, and #2 was the wild-type protein.

Reporting for specific materials, systems and methods

We require information from authors about some types of materials, experimental systems and methods used in many studies. Here, indicate whether each material, system or method listed is relevant to your study. If you are not sure if a list item applies to your research, read the appropriate section before selecting a response.

Materials & experimental systems

n/a	Involved in the study
☒	☐ Antibodies
☒	☐ Eukaryotic cell lines
☒	☐ Palaeontology and archaeology
☒	☐ Animals and other organisms
☒	☐ Human research participants
☒	☐ Clinical data
☒	☐ Dual use research of concern

Methods

n/a	Involved in the study
☒	☐ ChIP-seq
☒	☐ Flow cytometry
☒	☐ MRI-based neuroimaging